

EVAPORATING PLANETESIMALS: A MODELLING APPROACH

Arielle Ann Hogan

Submitted to the faculty of the University Graduate School
in partial fulfillment of the requirements
for the degree
Master of Science
in the Department of Geology,
Indiana University

October 2021

Accepted by the Graduate Faculty of Indiana University, in partial fulfillment of the requirements for the degree of Master of Science.

Master's Thesis Committee

Catherine A. Macris, Ph.D., Chair

Gregory K. Druschel, Ph.D.

Andrew P. Barth, Ph.D.

© 2021

Arielle Ann Hogan

DEDICATION

To Petra Batek, with gratitude.

ACKNOWLEDGEMENT

First and foremost, I would like to acknowledge my supervisor, Dr. Catherine Macris. I give her endless thanks for her support, patience, and far-reaching kindness. For providing me with advice and feedback to help me become a better thinker, writer, and scientist, all without ever causing me self-doubt. Her commitment to her student's success and well-being is genuine and truly felt—I am grateful to have been one of them.

Another special thanks goes to the brilliant Dr. Edward Young, for the many hours spent explaining (and re-explaining) complex concepts to me, without a hint of exasperation. It has been a privilege to work alongside you over the course of the past two years, during which I have gained invaluable insight. Thank you to the NASA Emerging Worlds Program for awarding Dr. Young and Dr. Macris the research grant that funded my position and made this project possible.

Other important thanks go to my committee members Dr. Gregory Druschel and Dr. Andrew Barth, for your time and input into this work. Your interest in my project from the beginning was wonderfully encouraging.

I would like to thank the other members of Dr. Macris' lab group, both past and present, for their help, support, and friendship. Ian Marrs, I am forever grateful the time you budgeted from your own life and research to help me in the lab. Ruiguang Pan, for your help in explaining programming to me step-by-step, when I was evidently in over my head. Emily Darling, I would like to thank you for your efforts in synthesizing the materials for this project, and for conducting the levitation experiments. While we have never had the fortune of meeting, your contribution is notable and much appreciated.

I have overwhelming gratitude for Eiríka Arnardóttir, who kept me accountable, and who supported me every day as both a student and a friend. You have been one of the most influential people on me these past two years, in the most positive way.

I would like to sincerely thank all of my friends and family that encouraged and supported me over the duration of my graduate degree, that list is limitless. In particular, my mother Holly and my stepfather Mike for proofreading my (admittedly) dense work.

Finally, I would like to thank my brother, Ben. Your eternally positive spirit kept me going when I didn't think I could. Thank you for inspiring me, and looking over me then, now, and always.

Arielle Ann Hogan

EVAPORATING PLANETESIMALS: A MODELLING APPROACH

This thesis is a comprehensive investigation into the mechanics of evaporation experienced by planetesimals during accretion, a planet-building process. The evaporation events that these rocky bodies experience govern their chemical evolution, impacting the chemistry of the final body – a planet. Studying these planet-building processes is notoriously difficult (e.g., Sossi et al., 2019). There are still many unknowns surrounding what controls the degree of evaporation these bodies experience, and the resulting chemical signatures. The current study was designed to attempt to define some important parameters that govern silicate melt evaporation.

Here, we isolate and evaluate the effects of (1) pressure, (2) oxygen fugacity and (3) the activity coefficient of MgO on evaporating planetesimals through a series of computational models. The model introduced in this study, the fO_2 Modified KNFCMAS Model, uses a robust stepwise routine for calculating evaporative fluxes from a shrinking sphere. The modelling results are then compared to data from partial evaporation experiments of synthetic chondrite spheres to demonstrate the validity of this model, and to expose unknowns about the physicochemical conditions of high temperature silicate melts experiencing evaporation (in this case, the effective pressure, and the activity coefficient of MgO). Major element-oxide and isotope data from the models yielded two main conclusions concerning planetesimals: (1) the rate of evaporation is controlled by pressure and oxygen fugacity and (2) the chemical composition of the residual melt is controlled by oxygen fugacity and the activity coefficient of MgO. Results from computational modelling and evaporation experiments were used to determine an

approximation for the activity coefficient of MgO in a simplified chondritic composition, as well as the effective pressure experienced by the evaporating spheres during the partial evaporation experiments. This study outlines the controls on planetesimal chemistry during evaporation and provides a more accessible means of studying these complex processes.

Catherine A. Macris, Ph.D., Chair

TABLE OF CONTENTS

LIST OF TABLES	xi
LIST OF FIGURES	xii
CHAPTER 1: INTRODUCTION	1
1.1 Planetesimal Accretion	1
1.2 Definition of the Problem	2
1.3 Goal of This Study	3
CHAPTER 2: BACKGROUND	5
2.1 Chondrites	5
2.1.1 Enstatite Chondrites and Terrestrial Planets	6
2.2 Relative Volatility of Elements	6
2.3 Evaporation Processes	8
2.3.1 Equilibrium Evaporation	9
2.3.2 Kinetic Evaporation	9
2.3.3 Evaporation of Planetary Bodies	10
2.4 Oxygen Fugacity	10
2.5 Activity Coefficients	13
2.6 Literature Review	15
2.6.1 Laboratory Experiments	15
2.6.2 Computational Modelling	19
CHAPTER 3: METHODS	23
3.1 Experimental Design	23
3.2 f_{O_2} Modified KNFCMAS Model	23
3.3 Computational Models	25
3.3.1 Pressure Series	26
3.3.2 Oxygen Fugacity Series	27
3.3.3 Activity Coefficient Series	27
3.4 Sample Synthesis	28
3.5 Sample Levitation	30
3.6 Sample Analysis	31
CHAPTER 4: RESULTS	34
4.1 Pressure Model Results	34
4.1.1 Chemical Composition	34
4.1.2 Isotopic composition	39
4.2 Oxygen Fugacity Model Results	41
4.2.1 Chemical Composition	42
4.2.2 Isotopic Composition	49
4.3 Activity Coefficient Model Results	50
4.4 Results from Levitation Experiments	54
CHAPTER 5: DISCUSSION AND CONCLUSIONS	57

5.1 Discussion of Pressure	57
5.2 Discussion of Oxygen Fugacity	58
5.3 Discussion of Activity Coefficient of MgO	60
5.4 Discussion of f_{O_2} Modified KNFCMAS Model for Sample Analysis	61
5.5 Suggestions for Future Work	63
5.6 Conclusions	64
APPENDICES	66
Appendix A: Raw f_{O_2} Modified KNFCMAS Model Data: Pressure Series	66
Appendix B: Raw f_{O_2} Modified KNFCMAS Model Data: Oxygen Fugacity Series	66
Appendix C: Raw f_{O_2} Modified KNFCMAS Model Data: Activity Coefficient Series..	66
Appendix D: Raw MC-ICPMS Data from Levitation Experiments	66
REFERENCES	67
CURRICULUM VITAE	

LIST OF TABLES

Table 3.1: Starting compositions for fO_2 modified KNFCMAS model.	25
Table 3.2: Input conditions for model runs 1-6.	26
Table 3.3: Input conditions for model runs 7-9.	27
Table 3.4: Input conditions for model runs 10-15.	28
Table 3.5: Starting compositions of synthetic spheres.	28
Table 3.6: The starting weights and diameters of the synthetic spheres used in the levitation experiments.	29
Table 3.7: Experimental conditions for levitation experiments.	31
Table 4.1: The final weight, resulting mass loss, Mg/Mg ₀ and Fe/Fe ₀ ratios and change in $\delta^{25}\text{Mg}$ and $\delta^{56}\text{Fe}$ of the synthetic chondrites post-levitation and evaporation.	54

LIST OF FIGURES

Figure 2.1: Classification scheme for the major meteorite groups.	6
Figure 2.2: Condensation temperatures of some common elements.	7
Figure 2.3: A $\log fO_2$ vs. temperature diagram (Frost, 1991).	12
Figure 4.1: The abundance of Na_2O , FeO , MgO , SiO_2 , Al_2O_3 and CaO (in the residual melt) vs. time during evaporation are shown for 1.00 bar, 0.5 bar, 0.33 bar, 2.00×10^{-2} bar, 2.00×10^{-5} bar and 2.00×10^{-8} bar.	36
Figure 4.2: The abundance of Na_2O , FeO , MgO , SiO_2 , Al_2O_3 and CaO (in the residual melt) during evaporation vs. time (normalized to 1) at a pressure of 1.00 bar and 2.00×10^{-8} bar.	37
Figure 4.3: The final composition (in Wt. %) following evaporation modelled at 1.00 bar and 2.00×10^{-8} bar.	38
Figure 4.4: The abundance of Na_2O , FeO , MgO , SiO_2 , Al_2O_3 and CaO (in the residual melt, normalized to 1) vs. time (normalized to 1) during evaporation at pressure at 1.00 bar and 2.00×10^{-8} bar.	39
Figure 4.5: $\delta^{25}Mg$, $\delta^{56}Fe$, $\delta^{29}Si$, and $\delta^{18}O$ isotope values vs. time during evaporation for 1.00 bar, 0.5 bar, 0.33 bar, 2.00×10^{-2} bar, 2.00×10^{-5} bar, and 2.00×10^{-8} bar.	41
Figure 4.6: Na_2O , FeO , MgO , SiO_2 , CaO , and Al_2O_3 abundances (in the residual melt) vs. time during evaporation are shown for oxygen fugacity's of IW-1, IW-3 and IW-5.	43
Figure 4.7: The abundance of Na_2O , FeO , MgO , SiO_2 , Al_2O_3 and CaO (in the residual melt) vs. time (normalized to 1) during evaporation at oxygen fugacities of IW-1, IW-3 and IW-5.	45
Figure 4.8: The final composition (in Wt. %) following evaporation modelled at an fO_2 of IW-1, IW-3, and IW-5.	46
Figure 4.9: The abundances of Na_2O , FeO , MgO , SiO_2 , Al_2O_3 , and CaO (in the residual melt, normalized to 1) vs. time during evaporation at an oxygen fugacity of IW-1, IW-3, and IW-5.	48
Figure 4.10: $\delta^{25}Mg$, $\delta^{56}Fe$, $\delta^{29}Si$, and $\delta^{18}O$ isotope values vs. time during evaporation are shown for oxygen fugacity's of IW-1, IW-3, and IW-5.	50
Figure 4.11: The mass of Mg (in the residual melt) relative to the initial mass of Mg (in the starting spheres), plotted against the mass of Fe (in the residual melt) relative to the initial mass of Fe (in the starting spheres) for activity coefficients of 0.05, 0.075, 0.1, 0.3, 0.7 and 0.9 for MgO	52
Figure 4.12: The abundance of Na_2O , FeO , MgO , SiO_2 , Al_2O_3 , and CaO (in the residual melt) vs. time (normalized to 1) during evaporation with an activity coefficient for MgO of 0.1, 0.3 and 0.7.	53
Figure 4.13: The mass of Mg relative to the initial mass of Mg , plotted against the mass of Fe relative to the initial mass of Fe	55
Figure 4.14: $\delta^{25}Mg$ vs. $\delta^{56}Fe$ during evaporation.	56

CHAPTER 1: INTRODUCTION

1.1 Planetesimal Accretion

The theory of planetesimal accretion, proposed by Thomas Chamberlin and Forest Moulton in 1905 (Fairbridge and Hetherington, 1997), has been widely accepted as a dominating mechanism in planet formation. Planetesimal accretion refers to the collision and coalescence of kilometer-scale rocky bodies in the rotating disk of debris around a young star, i.e., the protoplanetary or accretionary disk. Gravitational influence between these rocky bodies in the midplane of the disk causes repeated violent collisions that form planetary “embryos” (de Vries et al., 2016). However, the process of planetesimal accretion alone is not sufficient to yield accretion at rates rapid enough for planetary growth within the timescale of a protoplanetary disk (Bitsch et al., 2019; Weidenschilling, 1977).

Recent discoveries of pebble-sized bodies in early planetary disks have inspired the idea that a phenomenon similar to planetesimal accretion, referred to as pebble accretion, is likely a notable contributor to planetary growth (Johansen and Lambrechts, 2017). Pebble accretion occurs when millimetre to centimetre (pebble)-sized fragments enter a larger body’s region of gravitational influence. When the pebble enters this region, it experiences a loss of angular momentum, causing it to spiral into the gravitational field and accrete onto the growing body (Bitsch et al., 2019). This mechanism, when occurring in conjunction with planetesimal accretion, increases the rate of accretion and yields growth timescales that fall within the lifespan of the disk (Johansen and Lacerda, 2010).

When rocky bodies collide during accretion, melting of these pebbles and planetesimals occur. When impact-induced melting is significant, isostatic readjustment causes a “magma ocean” to encompass the entire surface of the pebble/planetesimal (de Vries et al., 2016), which then leaves it vulnerable to evaporation into space. These evaporation events result in mass loss and produce specific chemical signatures. Due to their large size, the gravitational field of planetary bodies would inhibit the amount of mass loss that is indicated by their chemical signatures. Instead, these mass loss events happened to smaller, and at least in part, molten, pebbles/planetesimals whose gravitational fields are sufficiently small to allow significant evaporation. The post-evaporation signatures that remain are then preserved in the final accretionary product – a planet (Young et al., 2019).

1.2 Definition of the Problem

While pebble/planetesimal accretion is becoming a widely accepted driver in planet formation, much is still unknown about the mechanics of the melting and evaporation events that these bodies experience during accretion. During evaporation, isotopic fractionation may occur whereby lighter isotopes are preferentially lost to the vapor phase, leaving a heavy isotope enrichment in the residual solid/melt. Our understanding of element partitioning and isotopic fractionation during planetesimal evaporation as a whole lacks support from a large body of experimental studies (Sossi et al., 2019). This is in part due to the fact that in natural samples (i.e., meteorites), the isotopic composition of the pre-evaporation body is unknown. Thus, the process of evaporation has only been studied indirectly using estimates based on the composition of meteorites following partial evaporation. In addition, when studying this process,

assumptions about the partitioning behaviour of elements are made based on relative volatilities defined by the 50% condensation temperatures of said elements. The 50% condensation temperature of an element, denoted as T_c^{50} , refers to the temperature at which 50% of its mass will have condensed from the vapour phase under solar nebula conditions (Lodders, 2003).

The solar nebula is the gaseous cloud from which our solar system originated. The conditions of the solar nebula consisted of a hydrogen rich atmosphere at 10^{-4} bar pressure. The 50% condensation temperatures alone should not be used to predict relative element volatilities under conditions *differing* from that of a solar nebula (e.g., pebble/planetesimal accretion in a proto-planetary disc). The processes of element partitioning and isotopic fractionation during planetesimal evaporation are remarkably complex and cannot be accurately represented by extrapolating behavior from the 50% condensation temperatures of the elements in question. In reality, element partitioning during planetesimal evaporation could be affected by many factors that will be discussed in detail in subsequent sections. These include oxygen fugacity, total pressure, vapor pressure at the melt-vapor interface, temperature, size of the evaporating body, flow surrounding the body, composition of the melt, and activities of species in the melt and gas. Since these evaporation events govern the chemical composition of a growing planetary body (and in turn, a planet), resolving the chemical controls in these systems is of significant relevance.

1.3 Goal of This Study

Using computational models, this study will implement a systematic investigation into the evaporation of planetesimals and isolate and evaluate the effects of parameters

responsible for the final chemistry of these bodies. These models will be compared to data from evaporation experiments to determine how they can be used to reveal physical conditions experienced by natural and synthetic samples. The ultimate goal is to advance our understanding of the physical and chemical evolution of planets, determine the controlling factors, and present a more accessible means of studying these processes.

CHAPTER 2: BACKGROUND

2.1 Chondrites

There are three main classes of meteorites: (1) chondrites, (2) primitive achondrites and (3) achondrites (Weisberg et al., 2006). The chondrite class is comprised of stony meteorites which contain chondrules, spherical once-molten inclusions of silicate from the early solar system. Of the three classes, chondrites are the most primitive form of meteorites as they did not experience melt differentiation (i.e., separation of a metallic core from silicate mantle) (Weisberg et al., 2006). Chondritic meteorites have compositions reflecting the early solar system (Young, 2017) and are extremely valuable in the study of planetary science and cosmochemistry as they provide insight into the initial components that were available in the early solar system (Weisberg et al., 2006). According to the planetesimal accretion theory, terrestrial planets initially formed from this early solar system material. Therefore, chondritic materials are thought to represent the initial composition of the Earth and likely make up a large contribution of the accretionary material (pebbles/planetesimals) involved in its formation. Chondrites are divided into three major classes based on compositions that suggest differing parent bodies: carbonaceous (C), ordinary (O), and enstatite (E). Amongst these major classes, chondrites are further classified into 15 groups (e.g., Weisberg et al., 2006). This classification scheme is shown in Figure 2.1.

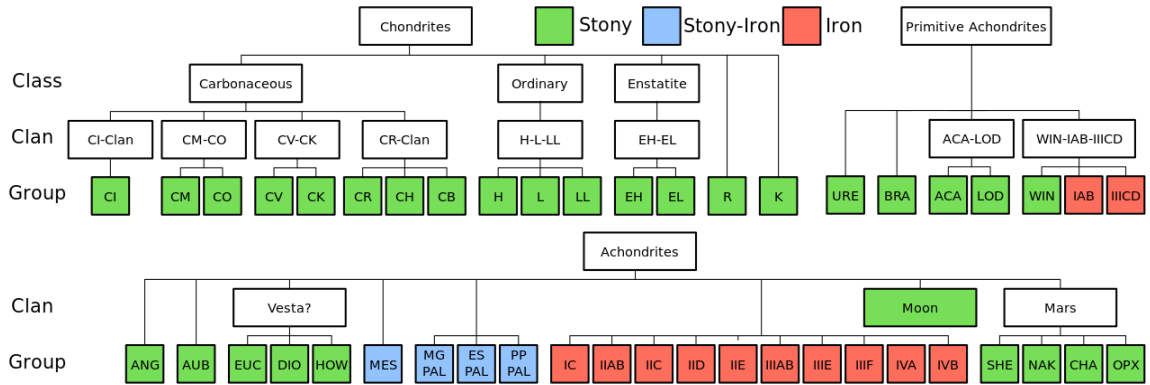


Figure 2.1: Classification scheme for the major meteorite groups. From Weisberg et al. (2006).

2.1.1 Enstatite Chondrites and Terrestrial Planets

Of the chondrite classes listed above, enstatite (E) chondrites are the most reduced (oxygen poor) class and are considered the most representative for the starting composition of Earth (Javoy et al., 2010). This is because enstatite (E) chondrites are the only class of chondrites with isotopic compositions matching that of Earth’s mantle (Javoy et al., 2010). Elements O, S, N, Mo, Ru, Ni, Cr, Ti, Fe, Os, Nd, Ca, Zn, Sr, and Mg all demonstrate isotopic signatures coequal in E chondrites and Earth’s mantle (Sikdar and Rei, 2020). This provides overwhelming evidence that enstatite chondrites were a large contributor to Earth’s starting materials. To ensure direct applications to Earth, compositions reflecting enstatite chondrites were chosen for this study.

2.2 Relative Volatility of Elements

As previously described, the 50% condensation temperature (T_c^{50}) of an element is specific to solar nebular conditions, however, condensation temperatures are widely used as a general way of describing the volatility of elements and how readily they will enter the gas phase (i.e., evaporate) relative to one another. Since the majority of the

literature referenced in this study uses this approach, some relevant definitions are provided below.

Volatile elements (VE) are those with condensation temperatures below ~1100 K, and thus often prefer the gaseous phase. Refractory elements (RE) have condensation temperatures above ~1500 K and thus often prefer the solid/condensed phase. Moderately volatile elements (MVE) exhibit condensation temperatures ranging from 1100–1300 K, while moderately refractory elements (MRE) have condensation temperatures between 1300 and 1500 K (as defined by Taylor, 2001). The condensation temperatures that are used to classify many common elements as refractory, moderately refractory, moderately volatile, and volatile are presented in Figure 2.1.

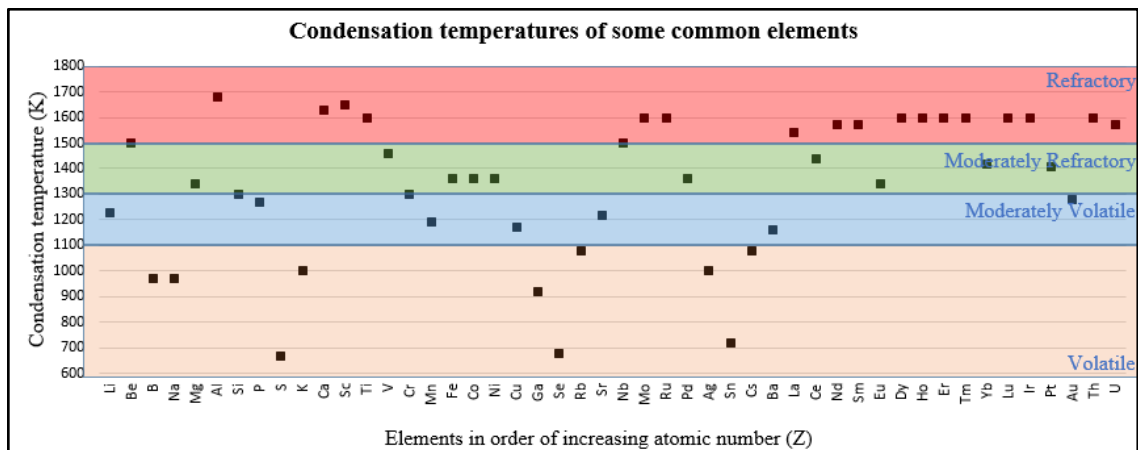


Figure 2.2: Condensation temperatures of some common elements, listed by order of increasing atomic number. The orange field encompasses elements defined as volatile, the blue field encompasses elements defined as moderately volatile, the green field encompasses elements defined as moderately refractory and the red field encompasses elements defined as refractory. Data taken from Taylor (2001).

In the case of volatile elements, their preference for the gas phase means that they are easily lost from a melt to evaporation, whereas refractory elements demonstrate the opposite behavior, tending to remain in the melt residue. Due to their intermediate

volatilities, moderately volatile (and some moderately refractory) elements show a more balanced partitioning in the event of evaporation (e.g., Sossi et al., 2019), and thus often experience isotopic fractionation due to partial evaporation – a process where the lighter isotopes of an element are preferentially lost to the gas phase, and heavier isotopes are preferentially retained in the condensed phase (i.e., the residual melt).

Fe is a moderately refractory element that demonstrates the balanced partitioning described above. It is also a valuable tracer isotope for planetary evolution, owing to its abundance in Earth, as well as its varying oxidation states (Fe^{3+} , Fe^{2+} and Fe^0). ^{57}Fe values are fairly consistent in chondrites at around 0 ‰, regardless of type (Sossi et al., 2016). Anything greater than this value is thought to be indicative of post-nebular fractionation (Sossi et al., 2016).

Mg is another moderately refractory element that exhibits balanced partitioning ideal for evaporation studies. Fe and Mg constitute some of the most common building block elements for Earth. They are therefore ideal choices for studying the process of fractionation that planetesimals experience during accretion.

2.3 Evaporation Processes

There are two end-members of evaporation processes: (1) equilibrium evaporation and (2) kinetic evaporation. Kinetic evaporation is also commonly referred to as “free evaporation” or “Langmuir evaporation”. Some natural processes, such as those of interest in this study, involve evaporation processes somewhere between these two end-members. These are described below.

2.3.1 Equilibrium Evaporation

Equilibrium evaporation occurs in a closed, chemically balanced system, where the forward and backward reactions (evaporation and condensation) are occurring at static rates, meaning the speed of these reactions remains constant over time. This is not to say that the isotope ratios of the two phases (vapor and condensed) are identical, but that the *relative* ratios of these phases remains the same over time (Kendall and Caldwell, 1998). Equilibrium evaporation may occur either congruently or incongruently. In the case of congruent evaporation, a compound (in this case a metal oxide) breaks down into either one (referred to as associative) or more (referred to as dissociative) species when phase change occurs. Regardless of how many species result, congruent equilibrium evaporation always maintains the same stoichiometry upon phase change (Sossi and Fegley, 2018). When this stoichiometry is not maintained between the condensed and gaseous phases, the evaporation is said to be incongruent. In order for any of the above forms of equilibrium evaporation to occur, the partial pressure of the vapor phase for a particular species must be equal to the partial pressure for that species at the surface of the condensed phase (Sossi and Fegley, 2018), thus requiring a closed system. In all other circumstances, the evaporation is, at least in part, kinetic.

2.3.2 Kinetic Evaporation

Kinetic evaporation, which occurs in an open system, does not maintain constant relative isotopic ratios between the vapor and condensed phases. This is because forward and backward reactions are not occurring at a static rate (the speed of the reactions will change over time), and in many cases some, if not all, of the produced vapor phase is removed from the system upon formation (Kendall and Caldwell, 1998). When the partial

pressure at the surface of the condensed phase is equal to zero, and none of the evaporated material re-condenses back into the melt, the evaporation process is purely kinetic. This condition can only exist under two circumstances: (1) when the evaporation is occurring in a vacuum, or (2) when the vapor phase is entirely removed from the condensed phase at a more rapid rate than it can be replenished (Sossi and Fegley, 2018). When melts are fractionated via kinetic evaporation, the melt experiences what is known as Rayleigh fractionation.

2.3.3 Evaporation of Planetary Bodies

When compared to chondritic precursors, silicate Earth displays a composition that is poor in volatile elements and one that is distinctly depleted in moderately volatile elements Pb, Tl, Zn, Sb, Bi and Ag (Norris and Wood, 2017). In addition, terrestrial planets show an enrichment of heavy Fe and Mg isotopes relative to their chondrite precursors. Earth also displays a heavy isotope enrichment of volatile element K (Wang and Jacobsen, 2016), as well as moderately volatile element Zn (Paniello et al., 2012) relative to CI chondrites, a subgroup of carbonaceous (C) chondrites. These distinct signatures are strong indicators of melt evaporation into space during planetary formation (Young et al., 2019). While these signatures lead to the confident conclusion that evaporation plays a significant role in planetary formation, the nature of the evaporation process and resulting elemental and isotopic signatures are still highly debated.

2.4 Oxygen Fugacity

Oxygen fugacity, denoted as fO_2 , refers to the non-ideal partial pressure of oxygen in a given environment (Albarède, 2011), or more simply, the availability of oxygen to react with other elements. In geosciences, oxygen fugacity is a variable that is

used to describe the plausibility of iron occurring in an oxidized vs. reduced state (Frost, 1991). A low (or negative) oxygen fugacity represents reducing conditions, such as those experienced in space, where iron occurs as pure iron metal, Fe⁰ (Frost, 1991). A high (or positive) oxygen fugacity represents oxidizing conditions, where iron occurs as Fe²⁺ and is readily incorporated into silicate minerals. At increasingly high oxygen fugacity, iron occurs as Fe³⁺ and is readily incorporated into magnetite and hematite, respectively. The reactions that dictate this speciation of iron are used to create a log oxygen fugacity (log *f*O₂) vs. temperature equilibria plot that is commonly referred to when quantifying oxygen fugacity. The main equilibrium reactions comprising this diagram are referred to as “oxygen buffers” and are shown below.

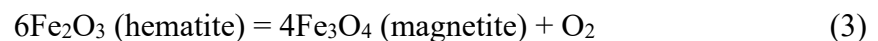
QIF:



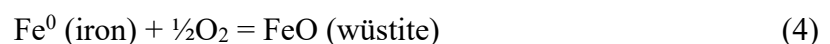
FMQ:



MH:



IW:



In short, oxygen fugacity describes the approximate availability of oxygen in mineral-forming environments, and thus, the likelihood of iron occurring as Fe^0 , Fe^{2+} or Fe^{3+} . To quantify oxygen fugacity means to measure the change in Gibb's free energy required to oxidize iron so that it changes from its reduced species to its oxidized species in an oxygen buffer reaction (Frost, 1991). As free energy is impacted by temperature, oxygen fugacity itself changes as a function of temperature. The oxygen fugacity (or free energy required to change from oxidized to reduced iron) of the oxygen buffers described above increases proportionally with increasing temperature. So, temperature must always be considered when discussing or attempting to quantify the oxygen fugacity of a given environment (Figure 2.2).

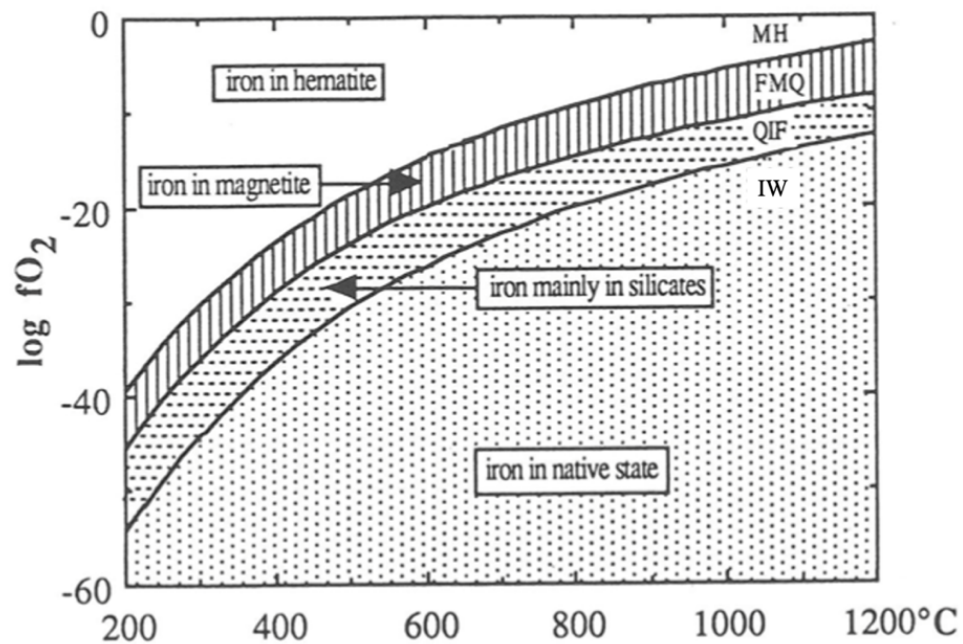


Figure 2.3: A $\log f_{\text{O}_2}$ vs. temperature diagram showing the relative stabilities of the various oxidation states of iron, and the resulting oxygen buffer reactions over oxygen fugacity space. Modified from Frost (1991).

The above oxygen buffers have been used to develop a shorthand way to describe oxygen fugacity at a given temperature. In literature, it is common to refer to the oxygen fugacity of an environment based on its value relative to one of the oxygen buffers. For instance, if at a known temperature, an environment is said to have an oxygen fugacity of $\log f_{\text{O}_2} - 1$ relative to the IW buffer, or a $\log f_{\text{O}_2}$ of IW-1, it is understood that this means the value for oxygen fugacity is 1 logarithmic unit below the IW buffer at that temperature. The IW buffer is almost exclusively used when discussing the highly reducing conditions in space where iron commonly exists as pure metal and is therefore the oxygen buffer that will be referred to in this study.

2.5 Activity Coefficients

In thermodynamics, the activity (a) of a species is a measure of the reactivity of that species in the mixture (Levine, 2019). It is a means of quantifying how the molecules of that species reacts with other molecules in a mixture (Druschel, G. personal communication, 2019). It is related to concentration by an *activity coefficient* (γ), a dimensionless quantity that describes the chemical potential of a substance (McNaught and Wilkinson, 1997). In non-ideal mixing of silicate melts, the activity of a species is related to the mole fraction of said species in the melt, via its activity coefficient:

$$a_i = \gamma_i X_i \quad (5)$$

Where a is the activity of species i , γ is the activity coefficient of species i and X is the mole fraction of species i in the melt.

The activity coefficient of a species in a given mixture is a variable thermodynamic property that describes the similarity (or dissimilarity) of atoms or molecules being mixed in a solution (Powell, 1978). The larger the activity coefficient,

the larger the difference between that molecule and other molecules in the mixture (Powell, 1978). The value for an activity coefficient can range from 0 to 1, depending on temperature, pressure, and the other species in the mixture, which makes it challenging to quantify in some natural processes. In MgO, SiO₂ and FeO-rich melts, such as the chondritic melts in this study, the activity coefficient of FeO is said to only be weakly dependent on composition (Wood and Wade, 2013), and thus, the FeO concentration should not significantly affect the activities of the other species in the melt (Alexander, 2002). However, the same cannot be said about MgO and SiO₂. The activity coefficients of MgO and SiO₂ are strongly dependent on composition (Wood and Wade, 2013), meaning the activity of MgO is highly influential on the activity of SiO₂— and vice versa.

Since FeO, MgO and SiO₂ are major rock-forming oxides, determining their activities under accretionary temperatures, pressures, and fO_2 conditions is of utmost importance. Numerous attempts have been made to constrain activity models for FeO, MgO and SiO₂. Satisfactory composition-dependent activity coefficient models have been developed for FeO (constrained by Wood and Wade, 2013) and SiO₂ (constrained by Young et al., 2019), but an appropriate model for the composition-dependent activity coefficient of MgO has yet to be developed. As a result, an activity coefficient of 1 for MgO is often used in silicate melt-vapor models, however this is the activity coefficient of MgO in an ideal gas and does not reflect non-ideal, natural systems. Such an oversimplification of natural systems can lead to misguided calculations for the chemistry of silicate melts.

2.6 Literature Review

2.6.1 Laboratory Experiments

Hin et al. (2017) showed evidence of evaporation through comparison of $^{25}\text{Mg}/^{24}\text{Mg}$ isotopes in Earth, primitive chondrite, and differentiated chondrite samples. Since the difference between $^{25}\text{Mg}/^{24}\text{Mg}$ in Earth is small relative to that in primitive chondrites, Hin et al. (2017), employs a “critical mixture double spiking” approach (rather than the common sample-standard bracketing approach) to resolve the relative abundances. The study found Earth (and other differentiated bodies) to have $^{25}\text{Mg}/^{24}\text{Mg}$ ~ 0.02 ‰ higher than chondrites. This $^{25}\text{Mg}/^{24}\text{Mg}$ enrichment is described as a result of evaporation-induced fractionation experienced by impact melts during accretionary growth.

Pringle et al. (2014) present Multi-Collector Inductively Coupled Plasma Mass Spectrometry (MC-ICPMS) data for $\delta^{30}\text{Si}$ from a suite of angrites, a rare type of achondrite with compositions reflecting alkali-depleted basalt (Keil, 2012). Angrites were chosen as they display significant Si isotope fractionation (with an average $\delta^{30}\text{Si}$ of -0.33 ± 0.12 ‰) when compared to chondrites, similar to that of terrestrial basalts. The angrite suite was measured and compared to the weighted average of chondrites (carbonaceous, ordinary, and enstatite) taken from pre-existing literature data. Pringle et al. (2014) describe the offset in $\delta^{30}\text{Si}$ as too significant for core formation to be the only responsible mechanism for fractionation. The redox conditions that would be required for the entirety of the observed fractionation are described as being unrealistic during core formation and thus likely result from evaporation during accretionary events. The results show that if planetesimals with initial volatile-rich compositions experienced impact-generated

melting and volatile loss through evaporation, then a final $\delta^{30}\text{Si}$ signature like that of angrites and terrestrial basalts would occur.

One of the shortcomings in the study of the chemical evolution of planets is the assumption of relative volatilities of elements as defined by their 50% condensation temperatures (e.g., Sossi et al., 2019). Norris and Wood (2017) addressed this with a series of volatile-loss experiments using doped basalt under a range of $f\text{O}_2$ conditions (10^{-7} atm to 10^{-13} atm) in a 1 atm gas-mixing furnace at 1300°C . The basalts were doped with Ag, Bi, Cd, Cr, Cu, Ga, Ge, In, Pb, Sb, Sn, Tl, and Zn oxides, and their volatilities and subsequent abundances as a function of oxygen fugacity were measured after heating. In this study, increasing volatilities of Cd, Ag, Cu, Ln and Zn (respectively) at an $f\text{O}_2$ of 10^{-7} atm was observed, which is inconsistent with the volatilities of these elements as defined by their 50% condensation temperatures. The results demonstrate the critical effect of environmental factors, such as pressure, temperature, and $f\text{O}_2$ on element volatilities and highlight the need to reconceptualise how relative volatility is defined. The study concluded that the results best representing the volatile element abundances in silicate Earth were volatilities observed at lower oxygen fugacities than solar gas conditions. They described post-collision partial melting and evaporation of bodies small enough where gravitational influence wouldn't inhibit the escape of vapor in the *absence* of solar gas (i.e., post-nebula) as the most appropriate explanation for Earth's volatile element abundances. This suggests that Earth's volatile element abundances are a product of accretion of these small bodies.

Sossi et al. (2019) developed a theoretical approach to understanding evaporation experienced by planetary bodies and how element loss through evaporation changes as a

function of time, temperature and oxygen fugacity. To do so, data was used from a series of experiments involving synthetic glasses with ferrobasic compositions ($\text{Fe}_2\text{O}_3\text{-MgO-Al}_2\text{O}_3\text{-SiO}_2 + \text{CaCO}_3$), that were doped with 20 elements (each at 1000 ppm): Li, Na, K and Rb in the form of carbonates and Cu, Ga, Ge, Pb, Mn, Mo, V, Zr, Sc, Zn, Ti, La, Gd, Yb, Ag and Cd as oxides. The study claimed that this ferrobasic reflected a composition similar to that of a planetary mantle. The synthetic ferrobasic was heated at temperatures ranging from 1300°C to 1550°C and was allowed to partially evaporate for times ranging from 15 to 930 minutes in a 1 atm gas-mixing furnace. The $f\text{O}_2$ conditions in the gas furnace ranged from 10^{-10} atm to $10^{-0.68}$ atm. The residual glasses were then quenched for compositional analysis. This study claims that the size of the furnace simulated an evaporation system that “approximated” open/kinetic evaporation. It suggested that the size allowed the evaporated species the opportunity to leave the “hot spot” and condense in the cooler region. The volatilities of the dopants were found to be highly dependent on $f\text{O}_2$, and the relative volatilities of Cr, Ga, Cu, Zn, Ge, Pb, Ag and Cd showed reasonable agreement to those of Norris and Wood (2017). Volatile elements, K and Na were found to becoming *increasingly* volatile at lower (more negative) oxygen fugacities.

Sossi et al. (2019) used this experimental data to develop a theoretical model (based on the Hertz-Knudsen-Langmuir theory) for quantifying the relative volatilities of elements in a silicate melt as a function of time, temperature and $f\text{O}_2$. The results showed a “near-binary” residual element distribution when melted at a single temperature and oxygen fugacity that clearly separated the volatile elements from the non-volatile elements. Sossi et al. (2019) state that while these results reflect what is observed for the moon and Vesta, it is not what is observed on Earth. Finally, they conclude that this

suggests accretion of pre-evaporated (volatile depleted) bodies. While this does provide even more support for pebble and planetesimal accretion, the intent of the model in the study was to extrapolate/predict element loss from silicate melts to study the effects of such processes on the chemical evolution of rocky bodies. However, in order to accurately conclude its relevance to Earth's formation, the study would ideally use a more realistic starting composition reflecting early planets (such as an undifferentiated chondrite).

Berthet et al. (2008) studied the effect of temperature and oxygen fugacity on phase equilibria in Indarch (EH4) chondrites at high pressures. This was done by partially melting a series of Indarch samples in a piston cylinder. The samples were doped with 0, 2, 4 and 6 wt% silicon metal to induce oxygen fugacities ranging from -1 to -5 (relative to the iron-wüstite buffer). All partial melting experiments were done at pressure of 1 Gpa (10,000 bar) and varied in temperature from 1200 to 1700 °C. Berthet et al. (2008) observed that more reducing environments directly correlated to higher melting points in the experimental environment, and they found that the lowest fO_2 (IW-5) experiments yielded liquidus temperatures ~100 °C higher than those at the highest fO_2 (IW-1). They noted that oxygen fugacity had a distinct effect on 1) olivine phase stabilization, in that it is more stable under oxidizing conditions, 2) SiO_2 phase stabilization, where it appeared to be more stable under reducing conditions when more silicon metal was present, and 3) monosulfides formed only under highly reducing environments (IW-4 to IW-5), indicating that the stability of sulfur is strongly reliant on the fO_2 conditions of the melt. Finally, the study concluded that redox conditions dominate the resulting nature of phase diagrams of high temperature Indarch melts. They state that this confirms the importance

of oxygen fugacity in the formation and resulting chemistry of planetary materials. The relationship between oxygen fugacity, thermodynamics and melt chemistry is clear in this study, however it would be irresponsible to simply assume that the same relationships could be extrapolated to low pressure conditions reflecting those experienced by planetesimals melting in space.

The evaporation studies discussed above show that the MVE-depleted signature observed in terrestrial planets was not obtained from the gradual degassing or core formation of a single body, but rather, is a cumulate of signatures obtained from various bodies that experienced differing degrees of melting/evaporation (Sossi et al., 2019). The bodies responsible for this accumulation of signatures are those that were involved in the pebble/planetesimal accretionary phase of planet formation. While the above studies contribute to our understanding of relative volatilities of these elements, there is still a deficit in experimental studies investigating evaporation during these early planetary processes. Some of the studies described above use a traditional gas-mixing furnace technique to simulate pure, kinetic evaporation. However, it should be noted that this is likely an oversimplification of natural evaporation systems. In natural systems, such as those involved in pebble/planetesimal accretion, some degree of recondensation from evaporative flux at the melt-vapor interface is likely to occur (Young et al., 2019), meaning the resulting evaporation is probably somewhere in between equilibrium and kinetic evaporation.

2.6.2 Computational Modelling

Computational models are commonly used to study the physics behind the formation of planetesimals. Carrera et al. (2017) modelled the evolution of debris belts

both with and without the formation of planetesimals from streaming instability. In planetesimal formation, the streaming instability is a radial drift effect caused by interacting streams of solid and gas with individual linear instabilities (Youdin and Goodman, 2005). The resulting radial drag modifies the orbital axes of the streaming material, causing drift towards a high-pressure region which could initiate planetesimal formation. (Youdin and Goodman, 2005). Through computational models, Carrera et al. investigated the probability of planetesimal formation from this effect during the evolution of debris belts. In doing so, Carrera et al. demonstrated that in order to achieve results with dust amounts consistent with observed debris belts, planetesimals must form.

Very few complex models have been presented on the chemical evolution of planetesimals from melting and evaporation. MAGMA is presently the most commonly used code for studying the vaporization of silicate melts. MAGMA is a silicate melt-vapor chemical equilibrium code developed by Fegley and Cameron in 1987. Fegley and Cameron developed this code to study iron and silicate fractionation of the Mercury protoplanet. Using both ideal and nonideal mixing models, they applied MAGMA code to model the vaporization of completely molten chondritic material ranging from 2500-3500 K.

Visscher and Fegley (2013) studied the Giant Impact Theory for the formation of the moon. They modelled impact-generated silicate melt evaporation ranging from 2000-4000 K using MAGMA code. Oxygen fugacity was then calculated using the outputs from these models. Visscher and Fegley report that high fO_2 values (i.e., highly oxidizing conditions) result for any disk atmosphere that is silicate in composition, due to the high abundance of oxygen in rock. They go further to say that any melt-vapor debris disk that

is a result of collision between rocky bodies is expected to have a high oxygen fugacity. The purpose of the study was to focus on the conditions during lunar formation. However, they state that the results are also applicable to collisions between any terrestrial planets where a debris disk containing silicate (in the melt and vapor) results from the impact.

Since its development, studies using MAGMA code have reported results that agree with experimental data (e.g., Schaefer and Fegley, 2004). Thus, it has been accepted as an appropriate means of modelling vaporization from silicate melts. MAGMA code uses a simple input for its algorithm. The code allows the user to input/vary the temperature of the evaporation environment, and the SiO_2 , MgO , Al_2O_3 , TiO_2 , Fe_2O_3 , FeO , CaO , Na_2O and K_2O abundances in the vaporizing melt. Upon completion, MAGMA presents activities of species in the melt, the associated activity coefficients, oxide mole fractions in the silicate melt, gas mole fractions and gas partial pressures. From these outputs, the oxygen fugacity of the theoretical melt can be quantified, however the oxygen fugacity of the vaporizing environment cannot be set or manipulated. In order for MAGMA to be directly applicable to both terrestrial igneous processes and extra-terrestrial processes, the oxygen fugacity of the melt-vapor environment would need to be able to be defined. The lack of available oxygen in space yields extremely reducing environments (Frost, 1991), which may lead to ramifications on the melt chemistry. At the very least, being unable to vary the oxygen fugacity in MAGMA inhibits the confirmation or refutation of this effect.

Furthermore, MAGMA is not intended to model spherical bodies. The kinetics of vaporization from a sphere are notably different than vaporization from a flat surface

(Eun, 2017). This is attributed to the size-dependent return flux of an evaporating sphere (Tang and Young, 2021) and the curvature effect (Brune, 2020). During evaporation, when the radius of a spherical body is greater than the mean free path of the molecules leaving its surface, then collision among the vapor molecules in the region immediately above the melt (known as the Knudsen layer) will cause a diffusive return flux (Young et al., 2019; Tang and Young, 2021). Thus, the size of a sphere will directly affect the evaporation mechanics under all conditions, as return flux will even be observed in vacuum (Anisimov, 1968). The curvature effect occurs when a curved surface experiences evaporation more readily than a flat surface due to the reduced availability of bonding at the surface of a sphere (Brune, 2020). This reduced bonding availability on spherical surfaces lessens the surface tension, which results in less energy required to facilitate evaporation. The curvature effect can be disregarded for planetary-size bodies, whose massive circumferences mean the “geometric horizon” is far enough away that it appears to be a plane from the perspective at the surface (Anderson, 1992). Such a phenomenon is experienced on the surface of Earth. Some reactions (e.g., evaporation) from such surfaces then, can be considered to be occurring on a plane. However, for spherical bodies with a radius less than 2mm, the rate of evaporation is inversely proportional to the radius (Morse, 1910). Thus, the curvature effect should be considered in the case of smaller pebbles and planetesimals, which can have radii ranging from km-scale down to mm-scale.

CHAPTER 3: METHODS

3.1 Experimental Design

A series of computational models were produced that simulate evaporation of enstatite chondrite composition planetesimals in a high-temperature flow regime. This is done in a systematic way to isolate the effects of single factors controlling the elemental and isotopic chemistry in these evaporative systems: (1) pressure, (2) oxygen fugacity and (3) the activity coefficient of MgO. We will compare the results of the models to experimental data from synthetic enstatite chondrites that have undergone partial evaporation. This approach is designed to test the validity of the computational models and to use them to learn about fundamental physicochemical properties of evaporating silicate melts in accretionary settings.

3.2. fO_2 Modified KNFCMAS Model

The model in this study uses an IDL+Fortran code first described by Young et al. (1998, 2019) and Shahar and Young (2007) to model evaporation from a CaO-MgO- Al_2O_3 - SiO_2 (CMAS) melt at the surface of an evaporating sphere. The mathematical model is based on a modified Hertz-Knudsen equation for calculating evaporative fluxes in a diffusive environment:

$$J_i = \frac{\gamma_i(P_{i,eq} - P_i)}{\sqrt{2\pi m_i RT}} \left(1 + \frac{\gamma_i r_o}{D_i^{gas}} \sqrt{\frac{RT}{2\pi m_i}} \right) \quad (6)$$

Where R is the gas constant, m_i is the mass of the species of interest (e.g., kg/mole), $P_{i,eq}$ is the equilibrium vapor pressure for the CMAS melt, P_i is ambient background vapor pressure of i , D_i^{gas} is the diffusion coefficient of i in the background gas (H_2), γ_i is the evaporation coefficient (dimensionless factor characterizing departures from the Hertz-

Knudsen equation), and r_o is the original radius of the evaporating object (Shahar and Young, 2007).

This code was modified by Tang and Young (2020) from a CMAS exclusive model to one that can include K, Na and Fe in the melt (referred to as the KNFCMAS model). The KNFCMAS model has been further modified for this study to allow for manipulation of oxygen fugacity in the input conditions, referred to hereafter as the fO_2 modified KNFCMAS model. This modified version allows specification of the following parameters for the starting conditions of the spheres and the evaporation environment: (1) radius of sphere, (2) starting composition of sphere, (3) temperature, (4) total pressure, (5) oxygen fugacity, (6) evaporation coefficients, and (7) activity coefficient for MgO.

The routine then uses these inputs to run a stepwise evaporation model for the evaporating sphere. When the model is complete (when Fe content reaches zero), it produces KNFCMAS oxide abundances from each step, as well as $\delta^{29}\text{Si}$, $\delta^{18}\text{O}$, $\delta^{25}\text{Mg}$, $\delta^{26}\text{Mg}$, $\delta^{56}\text{Fe}$ and $\delta^{57}\text{Fe}$ isotope values. The delta (δ) values produced by the model are a measure of the isotope concentration (in ‰) at each step of evaporation, subtracted by the initial concentration (in ‰) of that isotope.

The model uses fixed activity coefficients for NaO and K₂O based on Sossi et al. (2019), and integrates a more complex, composition-dependent model to calculate the activity coefficients for FeO:

$$RT\ln\gamma_{\text{FeO}} = -18994 + 99579X_{\text{Na}} + 192553X_{\text{Al}}X_{\text{Si}} + 282789X_{\text{Ca}}X_{\text{Mg}} + 79492X_{\text{Ca}}^2 + 120972X_{\text{Fe}}^2 \quad (7)$$

Where R is the ideal gas constant, T is temperature and X is the mole fraction of the oxide component (Wade & Wood, 2013). The model also uses a composition-dependent model for calculation of the activity coefficient of SiO_2 :

$$J_{\text{SiO}} = J_{\text{SiO}}^{\text{ref}} \frac{x_{\text{SiO}_2}}{x_{\text{SiO}_2}^{\text{ref}}} \exp \left[\frac{-2Wx_{\text{SiO}_2}}{RT} \left(\frac{x_{\text{SiO}_2}}{x_{\text{SiO}_2}^{\text{ref}}} - 1 \right) \right] \quad (8)$$

where W is the symmetrical interaction parameter, the subscript “ref” refers to the reference fluxes reported in literature, X is the mole fraction for the oxide component, R is the ideal gas constant and T is temperature (Young et al., 2019). Using experimental data, $-2Wx_{\text{SiO}_2}/(RT)$ is determined to approximately equal 8 and is thus simplified to 8 in the $f\text{O}_2$ modified KNFCMAS model.

All model iterations in this study were executed on a laptop using the Interactive Data Language (IDL) Platform, a programming platform by Harris Geospatial that has the ability to run Fortran and IDL codes together.

3.3 Computational Models

I conducted three series of models to isolate the effects of (1) total pressure, (2) oxygen fugacity and (3) the activity coefficient of MgO on the chemistry of evaporating planetesimals. The starting compositions of the spheres in all of the $f\text{O}_2$ modified KNFCMAS models reflected that of an enstatite chondrite, simplified to KNFCMAS components (Table 3.1).

Table 3.1: Starting compositions for $f\text{O}_2$ modified KNFCMAS model.

Oxide	Wt% ^(a)
FeO	27.754940
SiO ₂	44.318260
Al ₂ O ₃	2.284845

Table 3.1
cont.

Oxide	Wt% ^(a)
MgO	23.950410
CaO	0.725441
Na ₂ O+K ₂ O	0.966107
Sum	100

^(a) Oxide abundances correspond to a simplified Indarch (EH4) enstatite chondrite composition that has been simplified to KNFCMAS components.

3.3.1 Pressure Series

The pressure series used (runs 1-6) a constant starting radius of 0.02 cm, a temperature of 1700 K, an oxygen fugacity of IW-1, and an activity coefficient of 0.1 for MgO. Total pressure was changed in each run, to isolate its effect on oxide abundances and isotope fractionation from 2.00×10^{-8} to 1.00 bar (Table 3.2).

Table 3.2: Input conditions for model runs 1-6.

Run	Starting Radius (cm)	Temperature (K)	Activity Coefficient for MgO	$\log f_{\text{O}_2}$ ^(a)	Pressure (bar)
1	0.02	1700	0.1	IW-1	1.00
2	0.02	1700	0.1	IW-1	0.50
3	0.02	1700	0.1	IW-1	0.33
4	0.02	1700	0.1	IW-1	2.00×10^{-2}
5	0.02	1700	0.1	IW-1	2.00×10^{-5}
6	0.02	1700	0.1	IW-1	2.00×10^{-8}

^(a) Values given for f_{O_2} represent logarithmic units below the IW buffer at 1700 K.

3.3.2 Oxygen Fugacity Series

The oxygen fugacity series (runs 7-9) used a constant starting radius of 0.02 cm, a temperature of 1700 K, a pressure of 2.00×10^{-2} bar, and an activity coefficient of 0.1 for MgO. Oxygen fugacity was changed in each run, to isolate its effect on oxide abundances and isotope fractionation (Table 3.3).

Table 3.3: Input conditions for model runs 7-9.

Run	Starting Radius (cm)	Temperature (K)	Activity Coefficient for MgO	$\log f_{\text{O}_2}^{(a)}$	Pressure (bar)
7	0.02	1700	0.1	IW-1	2.00×10^{-2}
8	0.02	1700	0.1	IW-3	2.00×10^{-2}
9	0.02	1700	0.1	IW-5	2.00×10^{-2}

^(a) Values given for f_{O_2} represent logarithmic units below the IW buffer at 1700 K.

3.3.3 Activity Coefficient Series

For the third series of models (runs 10-15), conditions reflecting the environment of the levitation experiments were used: a constant starting radius of 0.1 cm, a temperature of 2307 K (an average of the temperatures in the levitation experiments), a pressure of 1.00×10^{-2} (an approximation of the *effective* pressure that the spheres may experience in a flowing gas), and an oxygen fugacity of IW-2. The activity coefficient for MgO was changed in each run, to isolate its effect on the chondrite chemistry and to compare with real experimental data to determine whether the model may be used to determine the activity coefficient of MgO in an evaporating silicate melt (Table 3.4).

Table 3.4: Input conditions for model runs 10-15.

Run	Starting Radius (cm)	Temperature (K)	Activity Coefficient for MgO	$\log fO_2^{(a)}$	Pressure (bar)
10	0.1	2307	0.050	IW-2	1.00×10^{-2}
11	0.1	2307	0.075	IW-2	1.00×10^{-2}
12	0.1	2307	0.100	IW-2	1.00×10^{-2}
13	0.1	2307	0.300	IW-2	1.00×10^{-2}
14	0.1	2307	0.700	IW-2	1.00×10^{-2}
15	0.1	2307	0.900	IW-2	1.00×10^{-2}

^(a) Values given for fO_2 represent logarithmic units below the IW buffer at 2307 K.

3.4 Sample Synthesis

Starting materials for evaporation experiments were synthetic enstatite chondrites, with compositions reflecting simplified Indarch (EH4) (Table 3.5). The compositions used for the inputs in the fO_2 modified KNFCMAS models (Table 3.1) were a further simplified (to KNFCMAS) version of this same composition. Reagent grade oxide powders were weighed, combined, and homogenized using a mortar and pestle.

Table 3.5: Starting compositions of synthetic spheres.

Element Oxide	Weight Percent ^(a)
SiO ₂	41.838660
Al ₂ O ₃	2.157204
Cr ₂ O ₃	2.671304
Fe ₂ O ₃	29.119730
MgO	22.610320
CaO	0.690507

Table 3.5
cont.

Element Oxide	Weight Percent ^(a)
Na ₂ O	0.821552
K ₂ O	0.090724
Sum	100

^(a) Oxide abundances correspond to a simplified Indarch (EH4) enstatite chondrite composition.

The homogenized enstatite chondrite powders (EH4) were placed in spherical depressions in a highly conductive copper hearth and fused through de-focused laser heating. This method allows for synthesis of samples in an oxygen-free container while experiencing minimal mass loss and contamination (Weber et al. 1996); conditions critical for these experiments. Each of the fused spheres were then placed in a modified Bond Air Mill, which increased their smoothness and symmetry to promote aerodynamic levitation. Finally, the spheres were sonicated in ultrapure H₂O to remove any loose particles from the milling and were then dried, measured (diameters), and weighed. The sample numbers, starting weights and measurements of these spheres can be found in Table 3.6.

Table 3.6: The starting weights and diameters of the synthetic spheres used in the levitation experiments.

Sample Number	Starting Sample Weight (mg)	Starting Sample Diameter (cm)
EL 2.37	7.750	1.65
EL 2.41	7.638	1.67
EL 2.42	12.938	2.17

Table 3.6
cont.

Sample Number	Starting Sample Weight (mg)	Starting Sample Diameter (cm)
EL 2.55	11.866	2.08
EL 2.59	10.602	2.03
EL 2.61	14.400	2.26

3.5 Sample Levitation

The levitation experiments were designed to mimic the process of planetesimal evaporation by subjecting synthetic samples with known compositions reflecting enstatite chondrites to super-liquidus temperatures while being surrounded by a flowing gas. This simulated condition may have occurred in the early Solar System when pebbles/planetesimals experienced evaporation in the flowing hydrogen rich gas of the protoplanetary disk (Tang & Young, 2020), causing shear between molten silicate and vapor in the presence of a flowing gas phase.

The 6 samples were partially evaporated while being heated by a 400-Watt CO₂ laser and levitated from below on a flow of gas issuing from a conical nozzle in an aerodynamic levitation laser furnace. Since the levitation is container-less, this technique allows for samples to be subjected to extremely high temperatures without contamination by or mass loss to a container. The gas-mixing capability of the furnace allows for controlled oxygen fugacity. Pure N₂ was chosen for the levitation gas. The inert behaviour of N₂ prevents it from reacting with the sample, making it an ideal choice for these experiments. The N₂ levitation gas, which flows around the levitating sample, promotes the removal of the vapor phase from the condensed phase as evaporation

occurs. The spheres were levitated at an ambient pressure of 1 bar and temperatures between 2000 °C–2050 °C for varying amounts of time (Table 3.7).

Table 3.7: Experimental conditions for levitation experiments.

Sample Number	Gas Composition	Gas Flow Rate (cc/min)	Temperature (°C)	Ambient Pressure ^(a) (bar)	Time (s)
EL 2.37	N ₂	284	2000	1.00	120
EL 2.41	N ₂	279	2050	1.00	200
EL 2.42	N ₂	313	2050	1.00	200
EL 2.55	N ₂	312	2000	1.00	30
EL 2.59	N ₂	315	2050	1.00	110
EL 2.61	N ₂	315	2050	1.00	200

^(a) The ambient pressure refers to the pressure in the levitation chamber, not the pressure experienced by the spheres while levitating.

3.6 Sample Analysis

Following levitation, the melt residues were weighed and measured, and percent mass loss was calculated for each run product. The melt residues were then sent to the E.D. Young Laboratory within the Department of Earth, Planetary and Space Sciences at University of California-Los Angeles (UCLA). The laboratory houses a ThermoFinnigan Neptune Multi-Collector Inductively Coupled Plasma Mass Spectrometer (MC-ICPMS).

In preparation for MC-ICPMS, Fe and Mg were extracted and purified from the melt residues using ion exchange chromatography in a Class 100 clean wet chemistry laboratory within the E.D. Young Laboratory. To first prepare the melt residues for chromatography, they were placed in metal jacketed digestion bombs with thick-walled Teflon[®] liners to ensure chemical inertness. The samples were tightly sealed in the

digestion bombs and dissolved using a 1:1 HF and HNO₃ solution at 230 °C for 72 hours. Once fully dissolved, the samples were evaporated in Savillex™ (a high-density Teflon®) vials at 120 °C until dry. The samples were then redissolved in aqua regia, a 1:3 mixture of HNO₃ and HCl, at 120 °C for 24 hours. They were then re-dried via Sallivex™ evaporation. Finally, the samples were once again dissolved a 1 N HNO₃ solution. The nitric acid ensured that all Fe in the solution existed in the same oxidation state (Jordan et al., 2019). Sample solutions were then ready to be loaded into the resin columns for ion-exchange chromatography.

A three-column technique was used for the ion-exchange chromatography in HEPA-filtered laminar flow boxes. The procedure for the purification of Mg followed Young et al. (2009) and Macris et al. (2013), and is described here. The columns used were PFA micro-columns measuring 120 mm × 4 mm, each with a 70 ml sample reservoir. The columns were filled with 1.5 ml of wet AG 50W-X12 Bio-Rad™ anion-exchange resin in a 200-400 mesh hydrogen form (Young et al., 2009). This particular resin was chosen as the 2.1 meq capacity results in a column capacity of 36 mg of Mg²⁺. The columns were washed, rinsed and cleaned with 0.5 N HF, ~18 MΩcm²/cm water and 6 N HCl, respectively, and resins were conditioned with 1 N HNO₃. A typical load on the column was approximately 50µg of Mg in 300 µl of 1 N HNO₃. 70 ml of 1 N HNO₃ was used to elute Mg from Al in the column. The eluted Mg was evaporated to dryness (using Sallivex™) and then redissolved in 2% HNO₃ for MC-ICPMS analysis.

For Fe, the purification procedure followed Jordan et al. (2019), which is described here. 1 mL of pre-cleaned wet Bio-Rad™ AG1-X8 anion exchange resin in a 200-400 mesh was added to the column. The resin was then cleaned in the column using

an 18 M MΩcm²/cm water, 1 N HNO₃, 18 M MΩcm²/cm water and 0.4 N HCl sequence to remove any pre-existing Fe. The column was conditioned with 5 mL of 6 N HCl, and samples were loaded into the columns in 0.5-1.0 mL of 6 N HCl. To elute non-iron elements, 8 mL of 6 N HCl was used. The remaining Fe was then eluted using 8 mL of 0.4 N HCl. This two-step elution was repeated again, to obtain Fe purity. The pure, eluted Fe was evaporated to dryness in Sallivex™ and redissolved in 2% HNO₃ for MC-ICPMS analysis.

The ThermoFinnigan Neptune MC-ICPMS is set up with 9 Faraday cups, all of which are equipped with 10¹¹Ω amplifier resistors that are capable of counting single ions (Macris et al., 2013). This yields high mass resolving power (appx. 12,000 at 10% transmission), which is ideal for the analysis of stable isotope ratios, such as Mg and Fe, which otherwise have interferences with C⁺ and CN⁺ (Macris et al., 2013) and ⁴⁰Ar¹⁴N⁺ and ⁴⁰Ar¹⁶O (Jordan et al., 2019). Mg samples were run in dry plasma mode and ²⁴Mg⁺ and ²⁶Mg⁺ isotopes were measured simultaneously by the Faraday cups. Fe samples were run in wet plasma mode and ⁵⁴Fe⁺, ⁵⁶Fe⁺, ⁵⁷Fe⁺, and ⁵⁸Fe⁺ isotopes were measured simultaneously by the Faraday cups.

CHAPTER 4: RESULTS

4.1 Pressure Model Results

The results from the pressure series, runs 1-6, are shown in Figures 4.1 through 4.5. Full data output from runs 1-6 can be found in Appendix A.

4.1.1 Chemical Composition

Figure 4.1 shows the effect of pressure on MgO, SiO₂, FeO, Na₂O, CaO and Al₂O₃ abundances (in Wt.% oxide) over time during the evaporation of a simplified Indarch enstatite chondrite. The models (runs 1-6) used a consistent radius of 0.02 cm and were run at 1700 K, a log f_{O_2} of IW-1 and with an activity coefficient for MgO of 0.1. Total pressure was changed in each run. Run 1 used a total pressure of 1.00 bar, run 2 used a total pressure of 0.5 bar, run 3 used a total pressure of 0.33 bar, run 4 used a total pressure of 2.00×10^{-2} bar, run 5 used a total pressure of 2.00×10^{-5} bar and run 6 used a total pressure of 2.00×10^{-8} bar (Table 3.2). For all elements, the rate of evaporation increases with decreased pressure. The time for total loss (completion of the model) of FeO, MgO and SiO₂ decreased from 12,500 minutes at a total pressure of 1.00 bar to 7,000 minutes at a total pressure of 0.5 bar, then to 5,500 minutes at 0.33 bar, then to 2,000 minutes at 2.00×10^{-2} bar, 2.00×10^{-5} bar and 2.00×10^{-8} bar.

Al₂O₃ and CaO showed the inverse relationship; they became more rapidly concentrated in the melt from 1.00 bar (max concentration at 12,500 minutes) to 0.5 bar (max concentration at 7,000 minutes), to 0.33 bar (max concentration at 5,500 minutes). At pressures 2.00×10^{-2} bar and above, a max concentration at 2,000 minutes was observed.

Na₂O experienced total evaporation on a shorter timescale than the other oxides. At a pressure of 1.00 bar, total loss of Na₂O occurred at ~14 minutes, at a pressure of 0.5 bar, total loss of Na₂O occurred at ~12 minutes, at a pressure of 0.33 bar, total loss of Na₂O occurred at ~10 minutes and at pressures of 2.00×10^{-2} bar, 2.00×10^{-5} bar and 2.00×10^{-8} bar, total loss of Na₂O occurred at ~6 minutes.

In Figure 4.2, time has been normalized to 1 to compare the chemical compositions (in Wt. % oxide) for the highest (1.00 bar) (a) and lowest (2.00×10^{-8} bar) (b) pressure models over the course of the evaporation. At both 1.00 bar (run 1) and 2.00×10^{-8} bar (run 6), loss of Na₂O and FeO began immediately, resulting to an increase in MgO, SiO₂, Al₂O₃ and CaO percentages in the melt. Loss of SiO₂ begins at time ~0.2 at 1.00 bar total pressure, and at time ~0.1 at 2.00×10^{-8} bar total pressure. Loss of MgO begins at time ~0.4 at a total pressure of 1.00 bar, and at a time of ~0.28 at a total pressure of 2.00×10^{-8} bar. The point of inflections (at which decrease of SiO₂ and MgO begins) match the time of FeO loss (to 0 Wt. %) in both models. With the onset of MgO and SiO₂ loss, Al₂O₃ and CaO become rapidly more dominant in the residual melt. This is shown by the steep upward slope in Wt. % for Al₂O₃ and CaO associated with the onset of a downward slope for MgO and SiO₂.

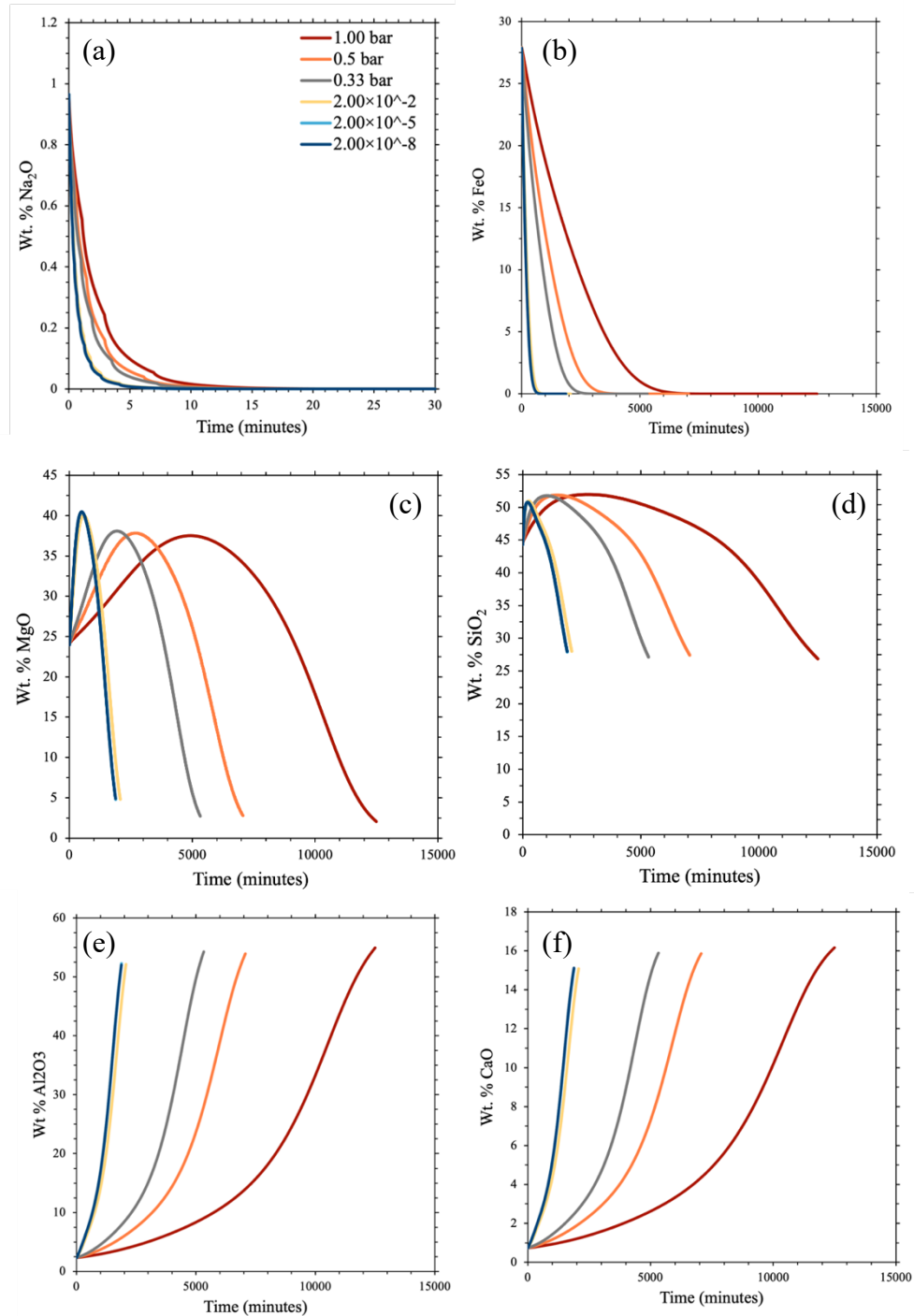


Figure 4.1: The abundance of Na₂O (a), FeO (b), MgO (c), SiO₂ (d), Al₂O₃ (e) and CaO (f) (in the residual melt) vs. time during evaporation are shown for 1.00 bar, 0.5 bar, 0.33 bar, 2.00×10^{-2} bar, 2.00×10^{-5} bar and 2.00×10^{-8} bar. The legend in graph (a) applies to all graphs in the figure. Note that Na₂O is displayed on a smaller time scale due to its rapid loss.

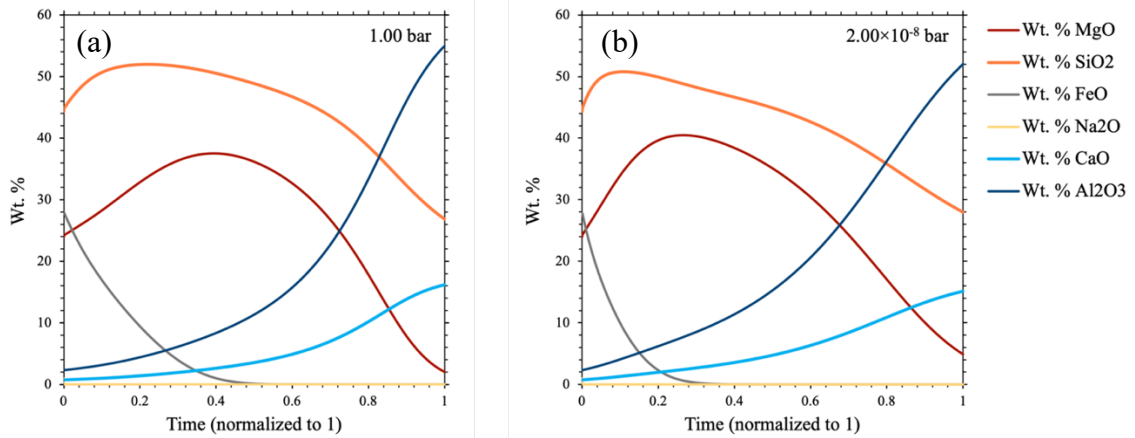


Figure 4.2: The abundance of Na₂O, FeO, MgO, SiO₂, Al₂O₃ and CaO (in the residual melt) during evaporation vs. time at a pressure of 1.00 bar (a) and 2.00×10⁻⁸ bar (b). Time has been normalized to a value of 1 for direct comparison. The legend on the right applies to both graphs in the figure.

The final composition upon completion of the models (when FeO goes to 0 Wt. %, shown as time = 1 on the graphs above) at a pressure of 1.00 bar and 2.00×10⁻⁸ bar are shown in Figure 4.3. The final abundances of Na₂O, FeO, MgO, SiO₂, Al₂O₃ and CaO observed in both the high pressure (1.00 bar) and low pressure (2.00×10⁻⁸ bar) runs are consistent; with only a 1.1 % discrepancy CaO, 1.2 % discrepancy for SiO₂, 2.9 % discrepancy for MgO and a 3.0 % discrepancy for Al₂O₃. Note that both models experienced complete loss of Na₂O and FeO.

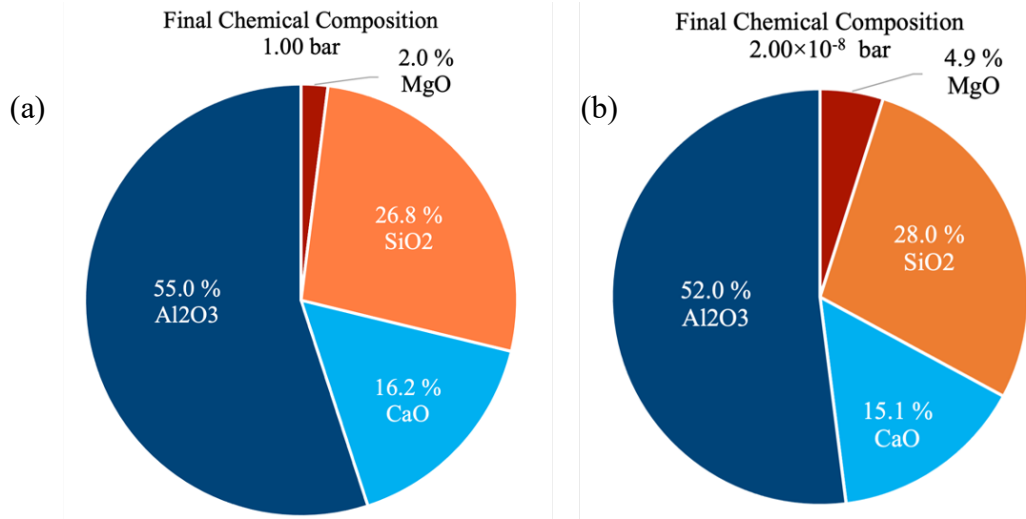


Figure 4.3: The final composition (in Wt. %) following evaporation modelled at 1.00 bar (a) and 2.00×10^{-8} bar (b). Note that both models show complete loss of FeO and Na₂O.

In Figure 4.4, time and weight percent have been normalized to 1 to directly compare the relative volatilities of oxides during evaporation in the highest (1.00 bar) and lowest (2.00×10^{-8} bar) pressure models. A volatility order of Na₂O > FeO > SiO₂ > MgO > Al₂O₃ > CaO is consistently observed for both high and low pressures. Inflection points for SiO₂ and MgO are inversely proportional to FeO loss at both 1.00 bar and 2.00×10^{-8} bar pressure, however the more rapid evaporation rate observed at 2.00×10^{-8} bar results in steeper negative slopes for SiO₂ and MgO following inflection. There is a switch in SiO₂ and MgO volatility, where MgO becomes more volatile than SiO₂, observed at Time = 7.45 at 1.00 and at Time = 0.8. The resulting volatility difference (space between the curves) following this switch is significantly less at 2.00×10^{-8} bar pressure, and the SiO₂ and MgO curves are near-equal for the remainder of the evaporation.

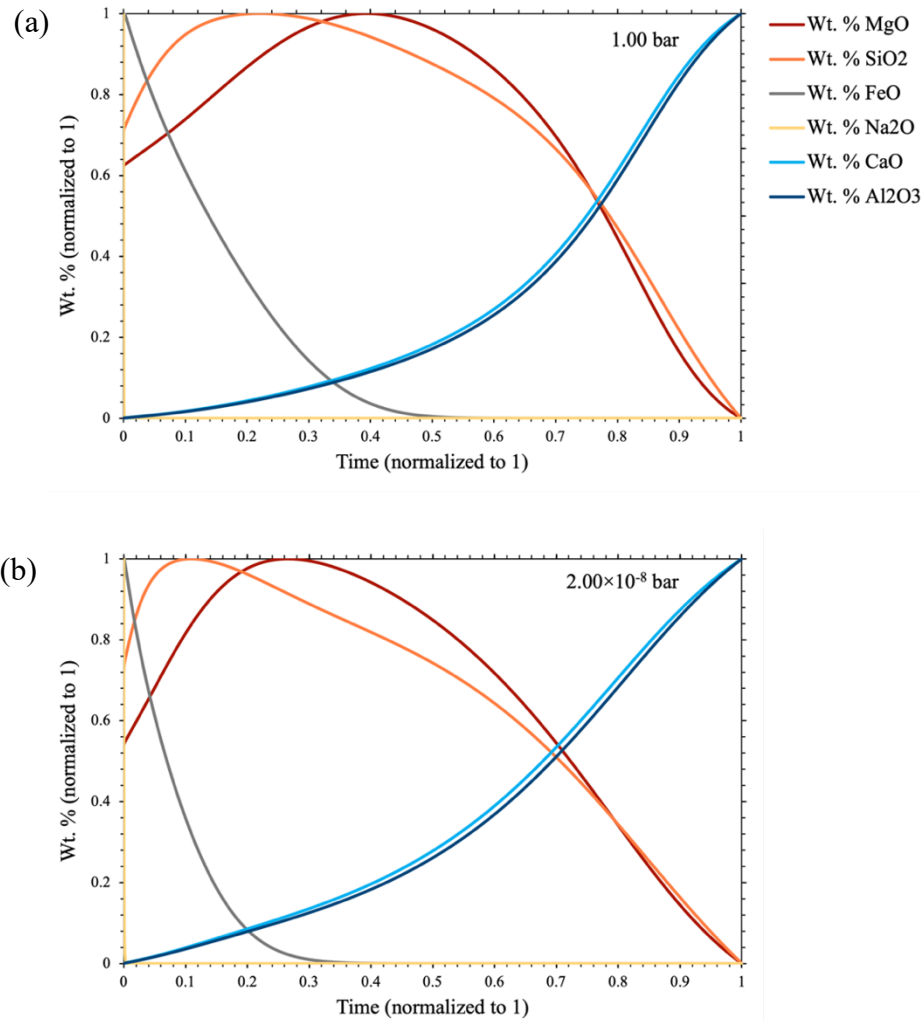


Figure 4.4: The abundance of Na₂O, FeO, MgO, SiO₂, Al₂O₃ and CaO (in the residual melt) vs. time during evaporation at pressure at 1.00 bar (a) and 2.00×10⁻⁸ bar (b). Time and Wt. % have been normalized to 1 for direct comparison of volatility. The legend for graph (a) applies to both graphs in the figure.

4.1.2 Isotopic composition

Figure 4.5 shows the effect of pressure on $\delta^{25}\text{Mg}$, $\delta^{56}\text{Fe}$, $\delta^{29}\text{Si}$, and $\delta^{18}\text{O}$ isotope values during the evaporation of a simplified Indarch enstatite chondrite. All isotopes show an increased rate of fractionation (steeper slope) with decreasing pressure. There is also a notable difference in the degree of fraction as a result of changing pressure. For all

isotopes, there is a higher degree of fractionation observed with decreasing pressure, up to 2.00×10^{-5} bar, where fractionation plateaus for all isotopes.

Upon completion of the 1.00 bar model (run 1), the final value for $\delta^{25}\text{Mg}$ was ~ 20 ‰, the final value for $\delta^{56}\text{Fe}$ was ~ 450 ‰, the final value for $\delta^{29}\text{Si}$ was ~ 6.5 ‰, and the final value for $\delta^{18}\text{O}$ was ~ 27.5 ‰. Upon completion of the 0.5 bar model (run 2), the final value for $\delta^{25}\text{Mg}$ was ~ 28 ‰, the final value for $\delta^{56}\text{Fe}$ was ~ 650 ‰, the final value for $\delta^{29}\text{Si}$ was ~ 12 ‰, and the final value for $\delta^{18}\text{O}$ was ~ 47.5 ‰. Upon completion of the 0.33 bar model (run 3), the final value for $\delta^{25}\text{Mg}$ was ~ 35 ‰, the final value for $\delta^{56}\text{Fe}$ was ~ 900 ‰, the final value for $\delta^{29}\text{Si}$ was ~ 14 ‰, and the final value for $\delta^{18}\text{O}$ was ~ 62.5 ‰. Upon completion of the 2.00×10^{-2} bar model (run 4), the final value for $\delta^{25}\text{Mg}$ was ~ 60 ‰, the final value for $\delta^{56}\text{Fe}$ was ~ 1900 ‰, the final value for $\delta^{29}\text{Si}$ was ~ 32.5 ‰, and the final value for $\delta^{18}\text{O}$ was ~ 155 ‰. Upon completion of the 2.00×10^{-5} bar and 2.00×10^{-8} bar models (runs 5 and 6), the final value for $\delta^{25}\text{Mg}$ was ~ 67.5 ‰, the final value for $\delta^{56}\text{Fe}$ was ~ 2150 ‰, the final value for $\delta^{29}\text{Si}$ was ~ 37.5 ‰ and the final value for $\delta^{18}\text{O}$ was ~ 175 ‰.

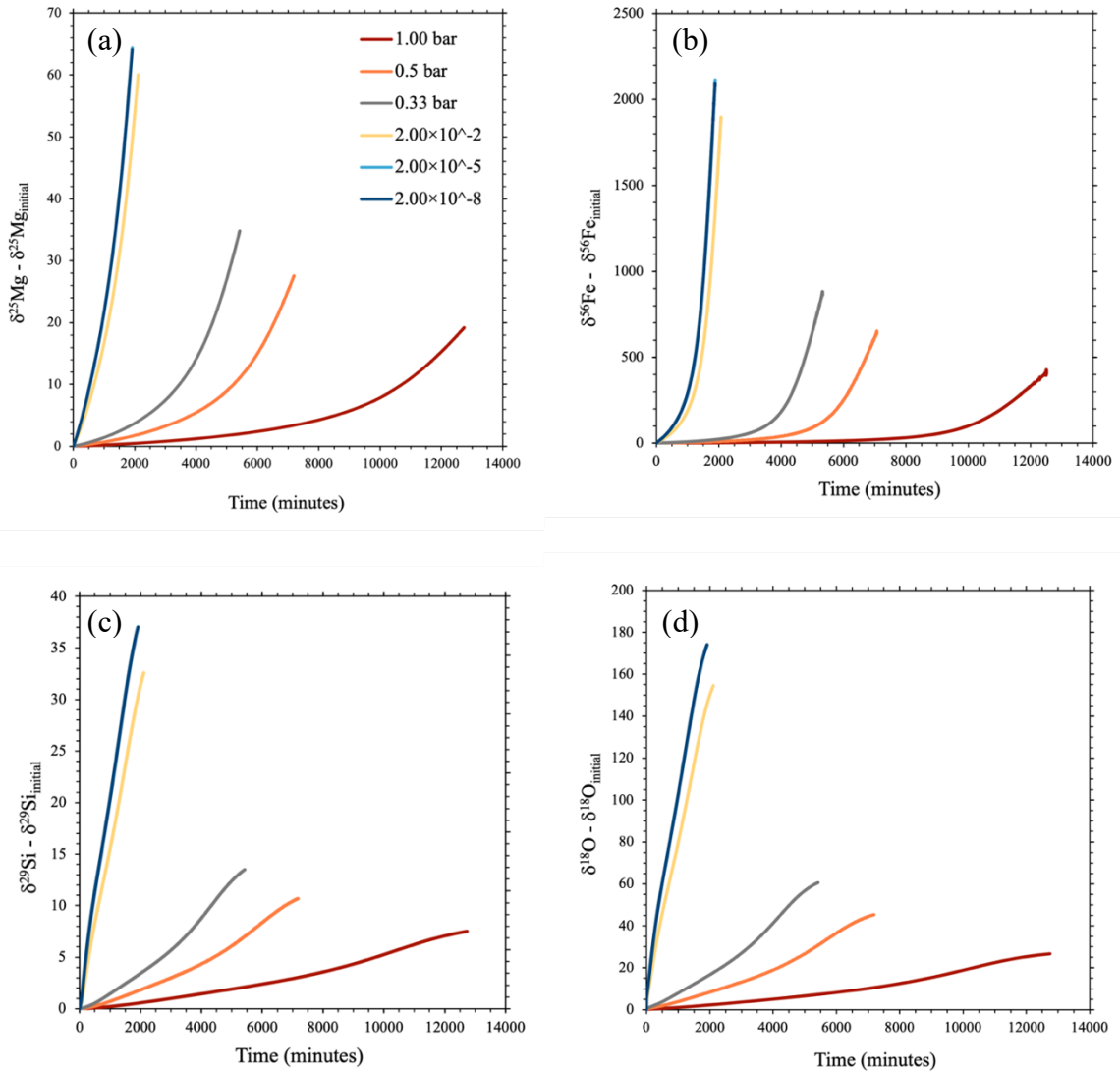


Figure 4.5: $\delta^{25}\text{Mg}$ (a), $\delta^{56}\text{Fe}$ (b), $\delta^{29}\text{Si}$ (c), and $\delta^{18}\text{O}$ (d) isotope values vs. time during evaporation are shown for 1.00 bar, 0.5 bar, 0.33 bar, 2.00×10^{-2} bar, 2.00×10^{-5} bar, and 2.00×10^{-8} bar. The delta values are represented as “isotope – isotope_{initial}” and thus the y-axis displays the change in isotope concentration (with respect to the starting concentration) over time. The legend for graph (a) applies to all graphs in the figure. Note that the scale for the y-axis changes for each isotope.

4.2 Oxygen Fugacity Model Results

The results from the oxygen fugacity series, runs 7-9, are shown in Figures 4.6–4.10. Full data output from the following models can be found in Appendix B.

4.2.1 Chemical Composition

Figure 4.6 shows the effect of oxygen fugacity on Na₂O, FeO, MgO, SiO₂, Al₂O₃ and CaO abundances (in Wt.% oxide) over time during the evaporation of a simplified Indarch enstatite chondrite. The models (runs 7-9) used a consistent radius of 0.02 cm and were run at 1700 K, with a total pressure of 2.00×10^{-2} bar and with an activity coefficient for MgO of 0.1. Oxygen fugacity was changed in each run. Run 7 used a $\log f_{\text{O}_2}$ of IW-1, run 8 used a $\log f_{\text{O}_2}$ of IW-3 and run 9 used a $\log f_{\text{O}_2}$ of IW-5 (Table 3.3) For all oxides, an increase in the rate of evaporation is observed as oxygen fugacity decreases (i.e. as conditions become increasingly reducing).

Time for total loss (completion of the model) of FeO, SiO₂ and MgO decreased from 2075 minutes at a $\log f_{\text{O}_2}$ of IW-1 to 175 minutes at $\log f_{\text{O}_2}$ of IW-3 to 25 minutes at a $\log f_{\text{O}_2}$ of IW-5. Al₂O₃ and CaO became increasingly concentrated in the melt during evaporation, and maximum concentration increased from 2075 minutes to 175 minutes to 25 minutes at $\log f_{\text{O}_2}$ of IW-1, IW-3, and IW-5 (respectively). Na₂O showed loss on faster timescales than the other oxides. Na₂O showed total loss by 8 minutes at a $\log f_{\text{O}_2}$ of IW-1, by 5 minutes at a $\log f_{\text{O}_2}$ of IW-3 and by 3 minutes at a $\log f_{\text{O}_2}$ of IW-5.

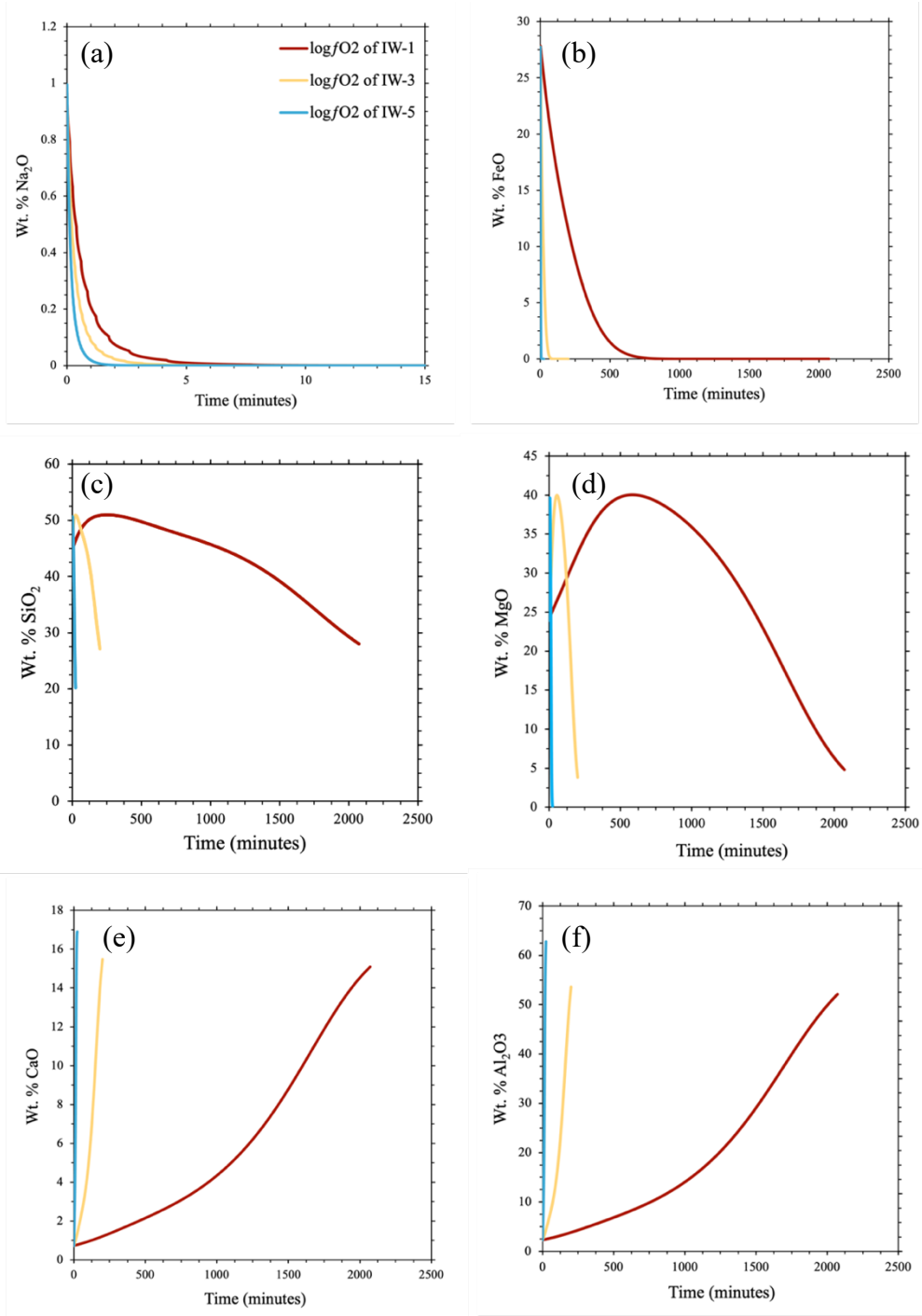


Figure 4.6: Na₂O (a), FeO (b), MgO (c), SiO₂ (d), CaO (e), and Al₂O₃ (f) abundances (in the residual melt) vs. time during evaporation are shown for oxygen fugacity's of IW-1, IW-3 and IW-5. The values for oxygen fugacity are relative to the iron-wüstite (IW) buffer at 1700 K. The legend in graph (a) applies to all graphs in the figure.

In Figure 4.7, time has been normalized to 1 to directly compare the final compositions (in Wt. % oxide) of the various oxygen fugacity runs. In all 3 models (runs 7-9), FeO and Na₂O loss begins immediately, resulting in increased concentrations (positive slope) of SiO₂, MgO, Al₂O₃, and CaO in the melt. Loss of SiO₂ begins at time = 0.12 (shown as an inflection point on the graph) for oxygen fugacities of IW-1 (run 7) and IW-3 (run 8), and at a time = 0.08 for an oxygen fugacity of IW-5 (run 9). The inflection point for MgO (the point at which MgO loss begins) is observed at a time of 0.3 for oxygen fugacities of IW-1 and IW-2, and at a time of 2.2 for and oxygen fugacity of IW-5.

Following the onset of MgO and SiO₂ loss, Al₂O₃, and CaO display rapidly increasing concentration in the residual melt, which is shown as a steep, positive slope for both oxides. The positive slopes for CaO and Al₂O₃ are slightly steeper for a log *f*O₂ of IW-5, which reflects the slightly steeper negative slopes for MgO and SiO₂ loss over time.

The final abundances of MgO, SiO₂, Al₂O₃, and CaO upon completion of the models (when FeO goes to 0 Wt. %, shown as time = 1 in Figure 4.7) at oxygen fugacities of IW-1, IW-3, and IW-5 are shown in Figure 4.8. The composition of the residual melts upon completion of the model (at time = 1) observed for *f*O₂ of IW-1 and IW-3 (a and b) vary significantly from those observed for IW-5 (c). The final abundance of Al₂O₃ increased from 52.1 % at a *f*O₂ of IW-1 and 53.6 % at IW-3 to 62.8 % at IW-5. The final abundance of CaO increased from 15.1 % to 15.5 % then to 16.9 % for a log *f*O₂ of IW-1, IW-3, and IW-5, respectively. The final abundance of MgO decreased from 4.8 % at a log *f*O₂ of IW-1 to 3.8 % at IW-3 to 0.1 % at IW-5. Loss in the final

abundance of SiO_2 was also observed with decreasing oxygen. At IW-1, the final abundance of SiO_2 was 28.0 %, at IW-3 the final abundance of SiO_2 was 27.1 %, and at a IW-5 the final abundance of SiO_2 was 20.2 %. All three models experienced complete loss of FeO and Na_2O .

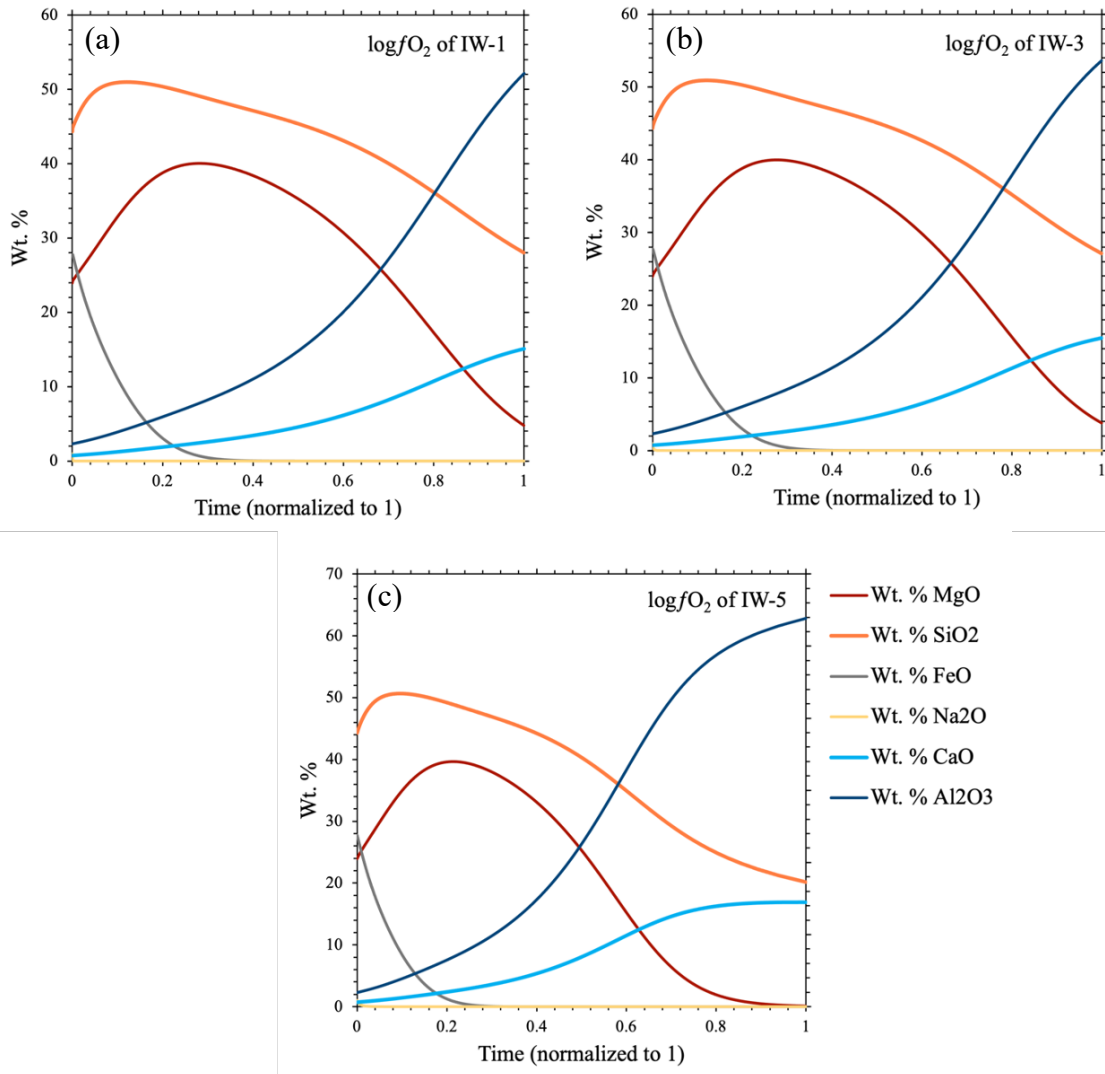


Figure 4.7: The abundance of Na_2O , FeO , MgO , SiO_2 , Al_2O_3 and CaO (in the residual melt) vs. time during evaporation at oxygen fugacities of IW-1 (a), IW-3 (b) and IW-5 (c). Values for oxygen fugacity are relative to the iron-wüstite (IW) buffer at 1700 K. Time has been normalized to 1 for direct comparison. The legend for graph (c) applies to all graphs in the figure.

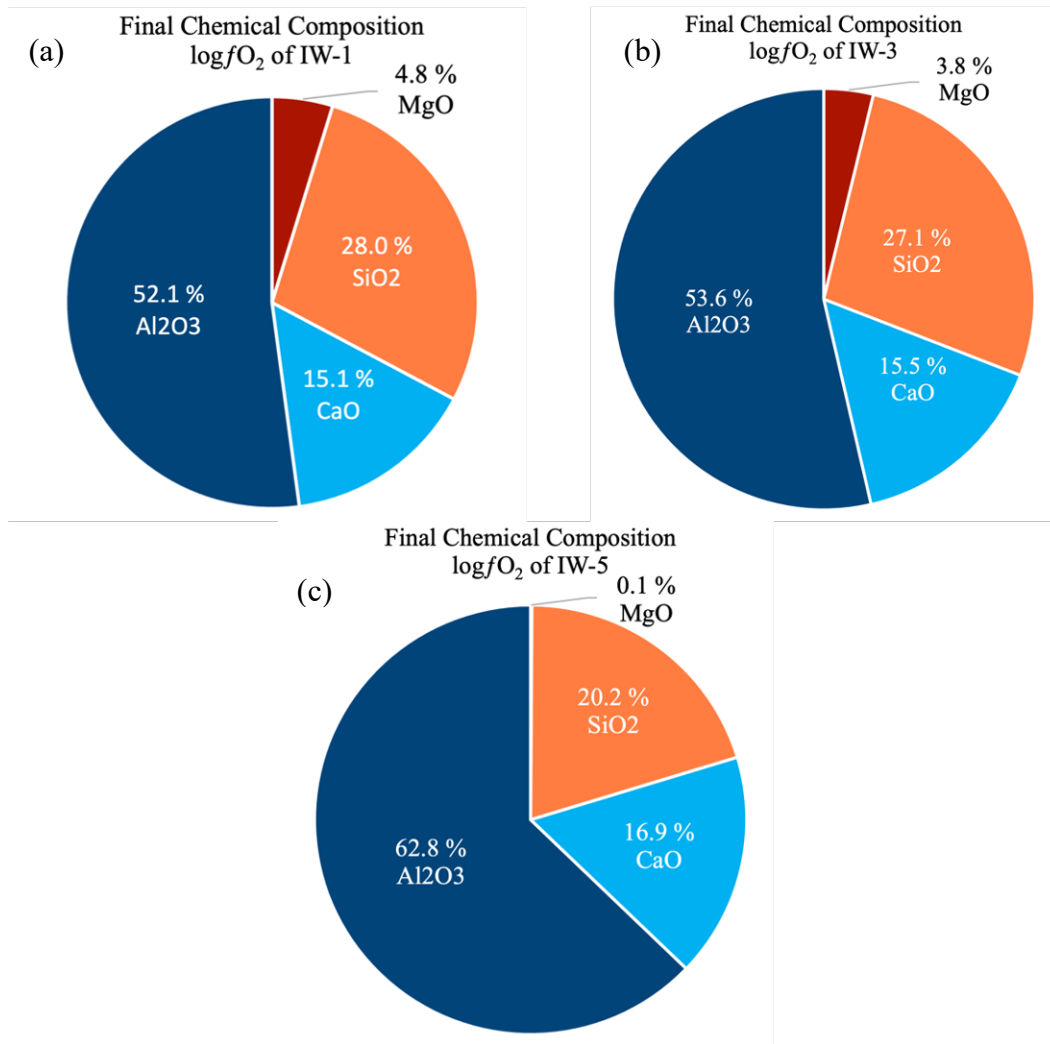


Figure 4.8: The final composition (in Wt. %) following evaporation modelled at an f_{O_2} of IW-1 (a), IW-3 (b), and IW-5 (c). Note that all models show complete loss of FeO and Na_2O .

In Figure 4.9, time and weight percent have been normalized to 1 to directly compare the relative volatilities of oxides over time during evaporation at the various oxygen fugacities. A volatility order of $NaO > FeO > SiO_2 > MgO > Al_2O_3 > CaO$ is consistently observed for oxygen fugacity's of IW-1 (a), IW-3 (b), and IW-5 (c). While the overall order of volatility remains the same in each model, there are notable changes in the volatilities of individual oxides with a change in oxygen fugacity. There is a

progressive decrease in the slope for Na_2O from a $\log f\text{O}_2$ of IW-1, to IW-3, to IW-5. The opposite behaviour is seen in the slope for FeO , which gets increasingly steeper with decreasing oxygen fugacity. There is also a notable change in the volatility crossover point for SiO_2 and MgO . For a $\log f\text{O}_2$ of IW-1, this switch in volatility (where the curve for SiO_2 crosses over the curve for MgO), is seen at time = 0.8. The two curves then remain nearly equal for the remainder of the model.

For a $\log f\text{O}_2$ of IW-3, The $\text{SiO}_2 - \text{MgO}$ volatility switch occurs at time = 0.76, after which point there is a discernable gap between the two curves for the duration of the model. The curves for CaO and Al_2O_3 remain equidistant in both models at IW-1 and IW-3. For a $\log f\text{O}_2$ of IW-5, the $\text{SiO}_2 - \text{MgO}$ volatility switch occurs at time = 0.47, after which there is a large gap between the two curves and the curve for SiO_2 remains significantly above that of MgO for the remainder of the model. There is also a much larger gap in the curves for CaO and Al_2O_3 at IW-5.

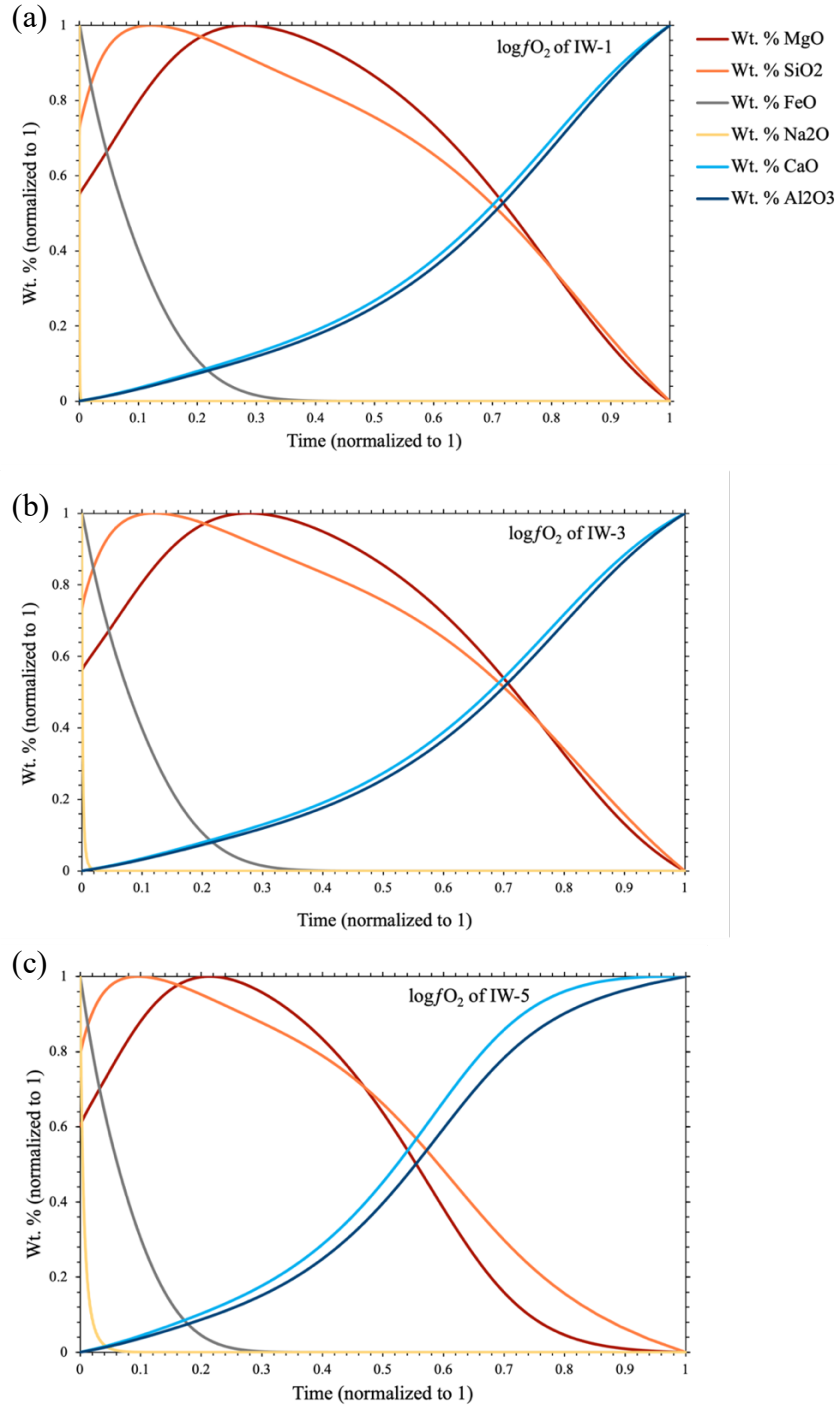


Figure 4.9: The abundances of Na₂O, FeO, MgO, SiO₂, Al₂O₃, and CaO (in the residual melt) vs. time during evaporation at an oxygen fugacity of IW-1 (a), IW-3 (b), and IW-5 (c). Values for oxygen fugacity are relative to the iron-wüstite (IW) buffer at 1700 K. Time has been normalized to 1 for direct comparison of volatility. The legend for graph (a) applies to all the graphs in the figure.

4.2.2 Isotopic Composition

Figure 4.10 shows the effect of oxygen fugacity on $\delta^{25}\text{Mg}$, $\delta^{56}\text{Fe}$, $\delta^{29}\text{Si}$, and $\delta^{18}\text{O}$ isotope values (in ‰) over time during the evaporation of a simplified Indarch enstatite chondrite. All isotopes show an increased rate of fractionation (steeper slope) with decreasing oxygen fugacity. There is also a notable difference in the degree of $\delta^{56}\text{Fe}$ and $\delta^{29}\text{Si}$ fraction resulting from a change in oxygen fugacity.

Upon completion of the model with a $\log f\text{O}_2$ of IW-1, The final value for $\delta^{25}\text{Mg}$ was ~62 ‰, the final value for $\delta^{56}\text{Fe}$ was ~1950 ‰, the final value for $\delta^{29}\text{Si}$ was ~33 ‰, and the final value for $\delta^{18}\text{O}$ was ~156 ‰. Upon completion of the model with a $\log f\text{O}_2$ of IW-3, the final value for $\delta^{25}\text{Mg}$ was ~65 ‰, the final value for $\delta^{56}\text{Fe}$ was ~1750 ‰, the final value for $\delta^{29}\text{Si}$ was ~33.5 ‰, and the final value for $\delta^{18}\text{O}$ was ~156 ‰. Upon completion of the model with a $\log f\text{O}_2$ of IW-5, The final value for $\delta^{25}\text{Mg}$ was ~123‰, the final value for $\delta^{56}\text{Fe}$ was ~1880 ‰, the final value for $\delta^{29}\text{Si}$ was ~37.5 ‰, and the final value for $\delta^{18}\text{O}$ was ~155 ‰.

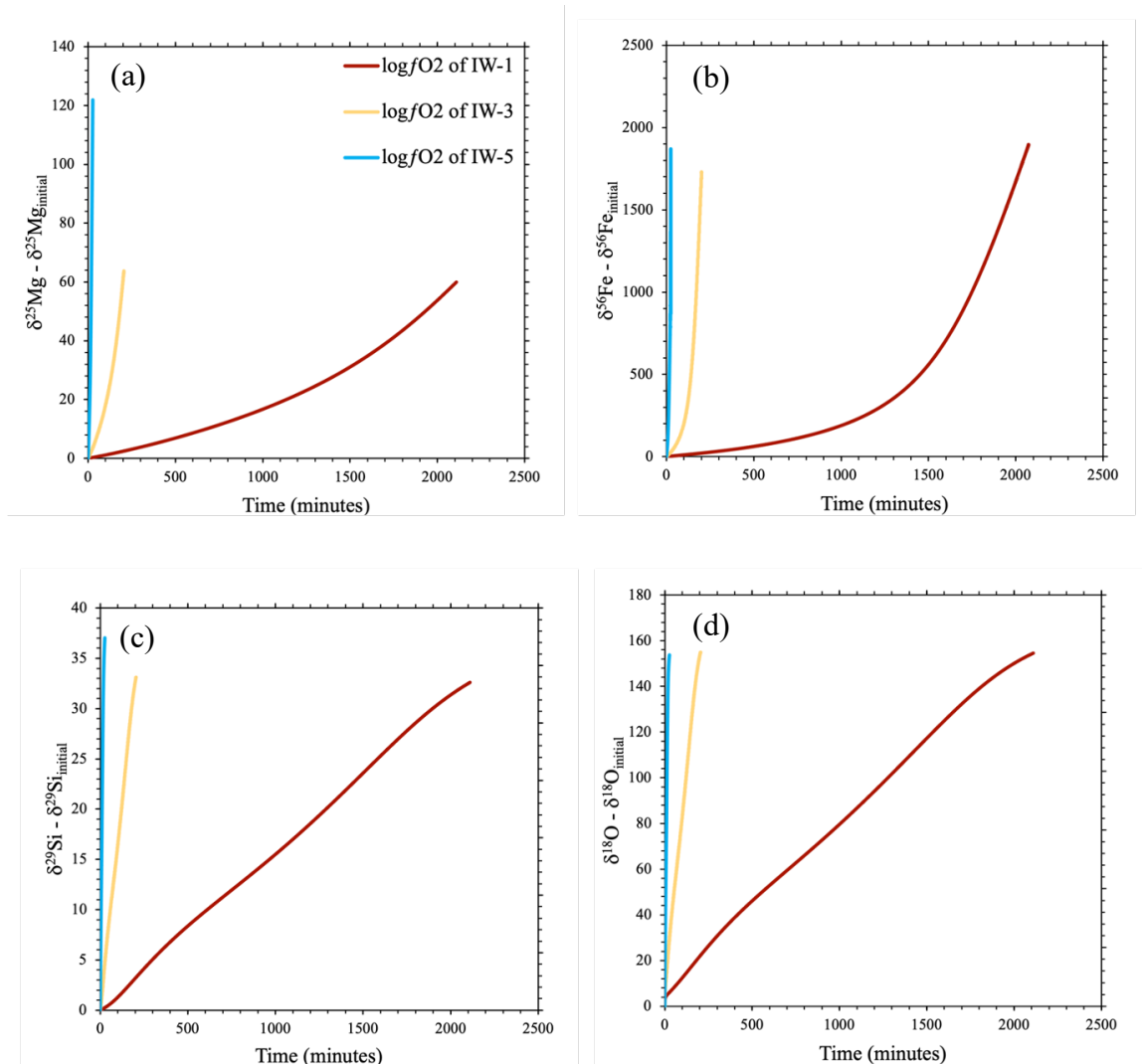


Figure 4.10: $\delta^{25}\text{Mg}$ (a), $\delta^{56}\text{Fe}$ (b), $\delta^{29}\text{Si}$ (c), and $\delta^{18}\text{O}$ (d) isotope values vs. time during evaporation are shown for oxygen fugacity's of IW-1, IW-3, and IW-5. The delta values are represented as "isotope – isotope_{initial}" and thus the y-axis displays the change in isotope concentration (with respect to the starting concentration) over time. Values for oxygen fugacity are relative to the iron-wüstite (IW) buffer at 1700K. The legend for graph (a) applies to all graphs in the figure. Note that the scale for the y-axis changes for each isotope.

4.3 Activity Coefficient Model Results

The results from the oxygen fugacity series, runs 10-15, are shown in Figures 4.11 and 4.12. Full data output from the following models can be found in Appendix C.

Figure 4.11 shows the effect of the activity coefficient of MgO on the masses of Fe (relative to the initial mass of Fe) and Mg (relative to the initial mass of Mg). The models (runs 10-15) used conditions that reflected the experimental environment: a consistent radius of 0.1 cm, a temperature of 2307 K, a total pressure of 1.00×10^{-2} bar and an oxygen fugacity of IW-1. The activity coefficient for MgO was changed in each run. Run 10 used an activity coefficient for MgO of 0.05, run 11 used an activity coefficient for MgO of 0.075, run 12 used an activity coefficient for MgO of 0.1, run 13 used an activity coefficient of 0.3, run 14 used an activity coefficient for MgO of 0.7, and run 15 used an activity coefficient for MgO of 0.9.

Each curve represents the relative concentrations of Fe and Mg in the melt over the course of evaporation. Thus, the slope of each curve describes the ratio of the activity of Fe in the melt to the activity of Mg in the melt. A concave downward slope is observed with an activity coefficient for MgO of 0.05, 0.075, 0.1, and 0.3, while a convex downward slope is observed for an activity coefficient for MgO of 0.7 and 0.9. There is a progressive decrease in slope for increasing activity coefficient for MgO.

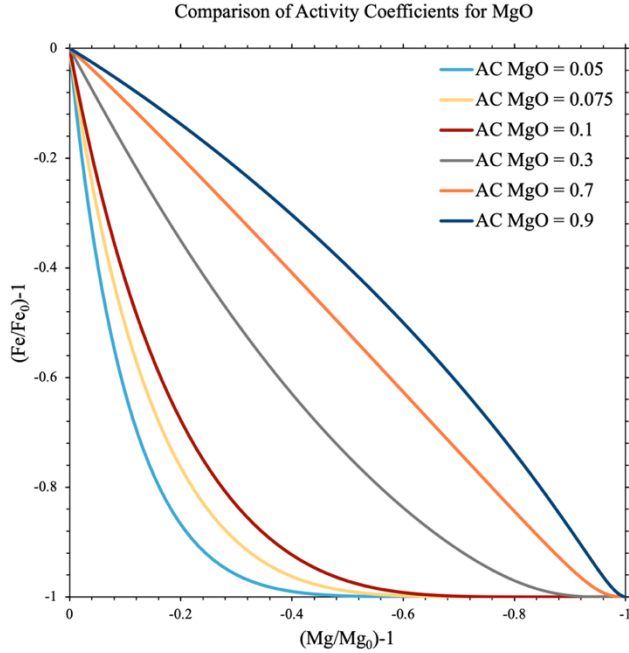


Figure 4.11: The mass of Mg (in the residual melt) relative to the initial mass of Mg (in the starting spheres), plotted against the mass of Fe (in the residual melt) relative to the initial mass of Fe (in the starting spheres) are displayed for activity coefficients of 0.05, 0.075, 0.1, 0.3, 0.7 and 0.9 for MgO. Both axes have been subtracted by one for better visual representation.

In Figure 4.12, time has been normalized to compare the Na_2O , FeO , MgO , SiO_2 , Al_2O_3 , and CaO abundances (in Wt. % oxide) for activity coefficient models for MgO of 0.1, 0.3, and 0.7. The abundances of MgO, SiO_2 , and FeO in the melts over the duration of the models varies significantly with changes in the activity coefficient of MgO. With an increase in the activity coefficient for MgO from 0.1 to 0.3, the volatility of FeO decreases and the slope of the curve for FeO becomes smaller. With an activity coefficient for MgO of 0.7, FeO is primarily retained in the melt, causing an inflection in the curve at time = 0.1, before gradually sloping downwards. The abundance of Na_2O , CaO and Al_2O_3 remain unchanged with a change in activity coefficient for MgO. With an increase in the activity coefficient for MgO from 0.1 to 0.7, the inflection point in the

curve for MgO shifts from time = 0.24 to time = 0.32, respectively. With an increase in the activity coefficient for MgO from 0.1 to 0.3, the SiO₂ curve displays a plateau from time = 0.08 to time = 0.32, before sloping downwards again. With an activity coefficient for MgO of 0.7, this plateau is enlarged from time = 0.1 to time = 4.4. The curves for Na₂O, CaO and Al₂O₃ remain unchanged in all 3 graphs.

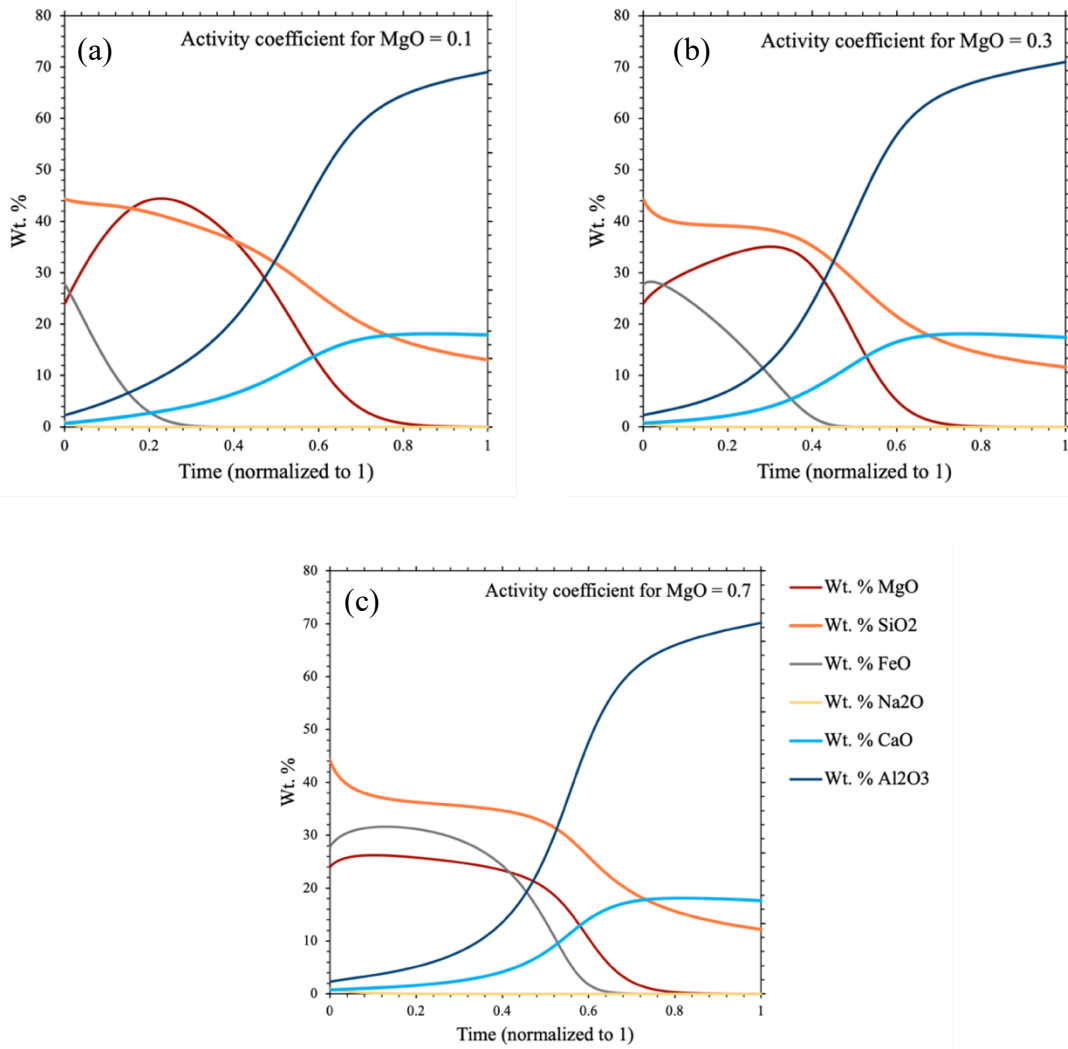


Figure 4.12: The abundance of Na₂O, FeO, MgO, SiO₂, Al₂O₃, and CaO (in the residual melt) vs. time during evaporation with an activity coefficient for MgO of 0.1 (a), 0.3 (b) and 0.7 (c). Time has been normalized to 1 for direct comparison. The legend for graph (c) applies to all graphs in the figure.

4.4 Results from Levitation Experiments

Laser heating of the spheres yielded varying degrees of fractionation and evaporative mass loss, the latter ranging from 4.8% to 36.1% (Table 4.1).

Table 4.1: The final weight, resulting mass loss, Mg/Mg₀ and Fe/Fe₀ ratios and change in $\delta^{25}\text{Mg}$ and $\delta^{56}\text{Fe}$ of the synthetic chondrites post-levitation and evaporation.

Sample Number	Final Sample Weight (mg)	Mass Loss (%)	Mg/Mg ₀ ^(a)	Fe/Fe ₀ ^(b)	$\delta^{25}\text{Mg}$ - $\delta^{25}\text{Mg}_{\text{initial}}$ (‰) ^(c)	$\delta^{56}\text{Fe}$ - $\delta^{56}\text{Fe}_{\text{initial}}$ (‰) ^(d)
EL 2.37	4.952	36.10	0.911	0.431	0.653	4.357
EL 2.41	7.084	7.25	0.969	0.929	0.076	0.355
EL 2.42	11.766	9.06	0.961	0.886	0.075	0.560
EL 2.55	11.296	4.80	0.984	0.995	0.090	0.104
EL 2.59	9.206	13.17	0.960	0.835	0.135	0.919
EL 2.61	12.784	11.22	0.964	0.861	0.078	0.812

^(a) Final mass of Mg in the melt residues/initial mass of Mg in the starting spheres, Mg₀, as measured by MC-ICP-MS.

^(b) Final mass of Fe in the melt residues/initial mass of Fe in the starting spheres, Fe₀, as measured by MC-ICP-MS.

^(c) MC-ICPMS measurements of the final concentration of $\delta^{25}\text{Mg}$ (in ‰) in the melt residues post-levitation, subtracted by the initial concentration of $\delta^{25}\text{Mg}$ (in ‰) pre-levitation.

^(d) MC-ICPMS measurements of the final concentration of $\delta^{56}\text{Fe}$ (in ‰) in the melt residues post-levitation, subtracted by the initial concentration of $\delta^{56}\text{Fe}$ (in ‰) pre-levitation.

The above data have been super-imposed on the models from runs 10-15 that used activity coefficients of 0.05, 0.75, 0.1, 0.3, 0.7 and 0.9 for MgO (Figure 4.13). When compared to the models, a linear trendline through the experimental levitation data shows an activity coefficient for MgO trending much smaller than 1. The MC-ICP-MS data from the levitation experiments can be found in full in Appendix D.

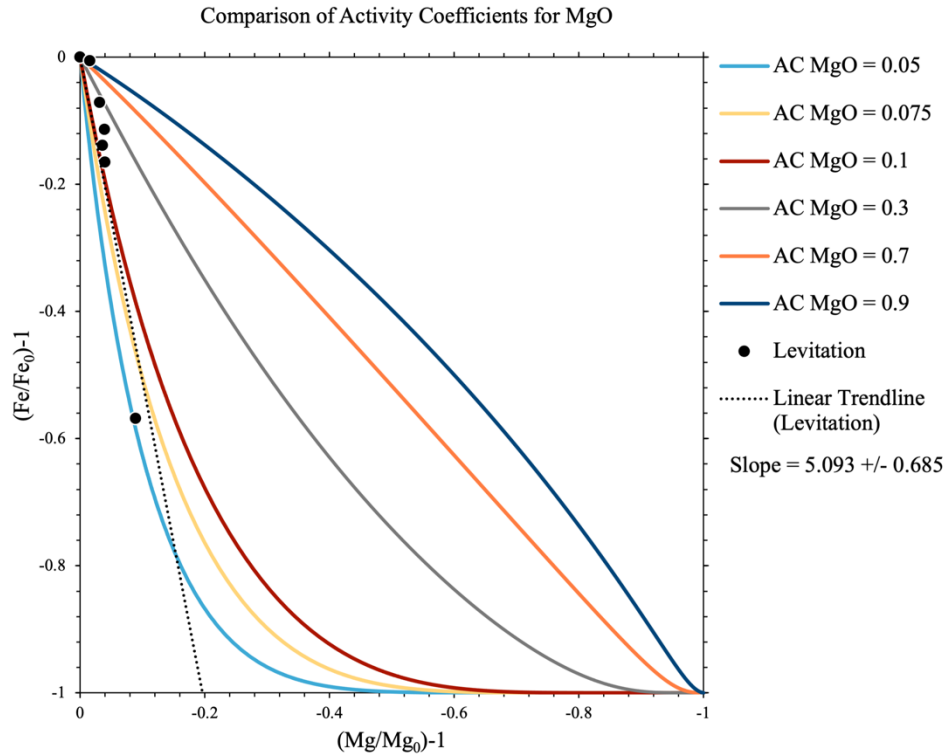


Figure 4.13: The mass of Mg relative to the initial mass of Mg, plotted against the mass of Fe relative to the initial mass of Fe. Both axes have been subtracted by one for better visual representation. The light blue, yellow, red, grey, orange, and dark blue lines represent activity coefficients of 0.05, 0.075, 0.1, 0.3, 0.7 and 0.9 for MgO, respectively. The experimental data are shown as black circles. The dashed black line is a linear trendline through the experimental data. The slope of the trendline and its associated uncertainty are displayed in the legend.

In Figure 4.14, MC-ICPMS measured $\delta^{25}\text{Mg}$ and $\delta^{56}\text{Fe}$ values for the experimental levitation samples (Table 4.1) have been superimposed on $\delta^{25}\text{Mg}$ and $\delta^{56}\text{Fe}$ values from models that used pressures of 0.01 bar, 0.1 bar, 0.33 bar, 0.5 bar, and 1.00 bar (Appendix A). When compared to the models, a line of best fit through the experimental levitation data shows a significantly steeper slope (corresponding to lower pressure) than the modelled projection of ^{25}Mg and $\delta^{56}\text{Fe}$ values at a pressure of 1.00 bar.

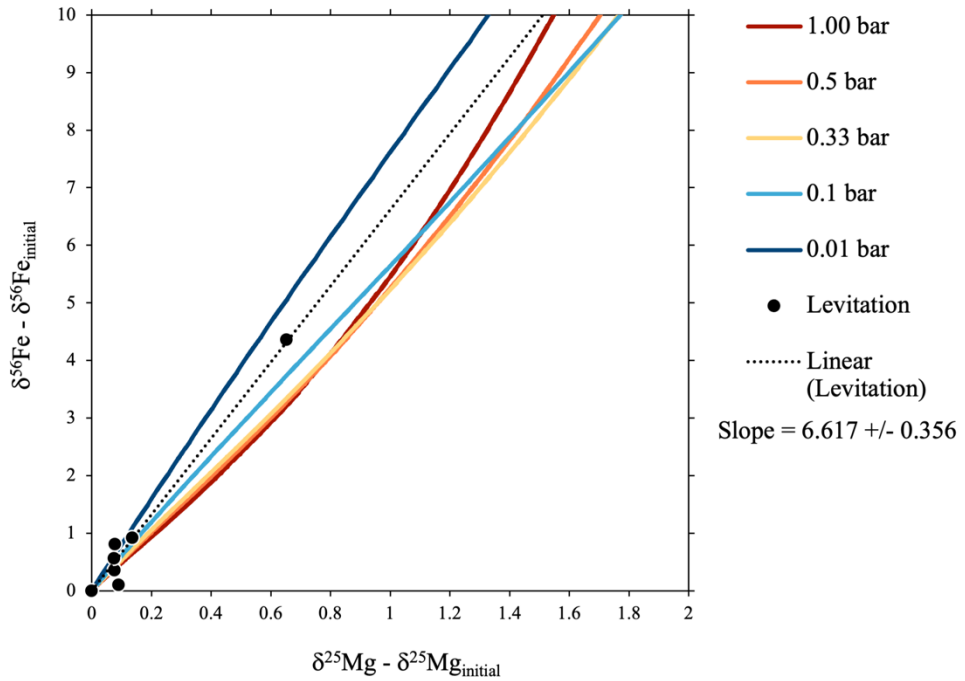


Figure 4.14: $\delta^{25}\text{Mg}$ vs. $\delta^{56}\text{Fe}$ during evaporation. The delta values are represented as “isotope – isotope_{initial}”, meaning the x-axis displays the change in $\delta^{25}\text{Mg}$ concentration in ‰ (with respect to the starting concentration, in ‰) over time, and the y-axis displays the change in $\delta^{56}\text{Fe}$ concentration in ‰ (with respect to the starting concentration) over time. Models run at pressures of 0.01 bar, 0.1 bar, 0.33 bar, 0.5 bar, and 1.00 bar are shown by dark blue, light blue, yellow, orange, and red lines, respectively. Experimental levitation data is displayed as black circles. A linear trendline, shown as a dashed black line, is applied through the levitation data. The slope of the trendline and its associated uncertainty are displayed in the legend.

CHAPTER 5: DISCUSSION AND CONCLUSIONS

5.1 Discussion of Pressure

The oxide and isotope results from the pressure models (runs 1-6) clearly show an increased rate of evaporation with decreasing pressure (Figures 4.1 & 4.5). According to thermodynamic principles, the boiling point of a liquid is the point at which the vapor pressure of the melt equals the total pressure (Geankoplis et al., 2018) At the boiling point, the liquid bonds reach maximum kinetic energy and evaporation readily occurs throughout the entire liquid body (Zuckerman, 2014). A reduction in total pressure will result in a lower vapor pressure required at the melt-vapor interface to reach the boiling point, thus encouraging earlier evaporation, and increasing the evaporation rate. This decrease in pressure with associated increase in evaporation rate effect seems to plateau at pressures above 2.00×10^{-2} bar, where maximum pressure-dependent evaporation rates of ~42 times that at 1.00 bar are achieved.

With this decrease in pressure and increase in evaporation rate, higher degrees of isotopic fractionation are observed (Figure 4.5). Again, this is attributed to the reduced vapor pressure at the surface of the melt required for evaporation at lower total pressures. Evaporation encourages the preferential escape of light isotopes, and thus, when the rate of evaporation is increased, an increase in isotopic fractionation in the melt is observed. This effect also plateaus at pressures below 2.00×10^{-2} bar.

The oxide abundances (Wt. %) do not appear to be significantly affected by the total pressure of the evaporation environment. While oxide loss happens on shorter time scales with increased evaporation rates (up to 625% faster from 1.00 bar to 2.00×10^{-8} bar), the final weight percent of oxides in the residues remain approximately the same

upon completion of the model. Even the most drastic differences in total pressure (1.00 bar vs. 2.00×10^{-8} bar), exhibit a maximum of 3 Wt. % difference in the final melt residue (Figure 4.3). The consistent volatility order of $\text{Na}_2\text{O} > \text{FeO} > \text{SiO}_2 > \text{MgO} > \text{Al}_2\text{O}_3 > \text{CaO}$ at all total pressures (Figure 4.4) suggests that pressure does not affect the relative volatilities of these major Earth-building oxides.

5.2 Discussion of Oxygen Fugacity

Oxygen fugacity also appears to be a significant control on the rate of evaporation. The oxide and isotope results show a significant increase in evaporation rate with a decrease in oxygen fugacity, with a rate of evaporation ~ 100 times higher at an oxygen fugacity of IW-5 than at IW-1 (Figures 4.6 & 4.10). This is consistent with Norris and Wood (2017), who found that the rate of evaporation of moderately volatile elements increased with more reducing conditions (a lower oxygen fugacity). The observed increase in rate of evaporation with lower oxygen fugacity is a speciation effect from the congruent evaporation of metal-oxides (Sossi and Fegley, 2018), where the metal-oxides break down into two or more species upon phase change. If the gas that results from this congruent evaporation is more reduced than the condensed species, then that metal-bearing gas will have a *higher* vapor pressure at the melt-vapor interface. If the resulting gas is more oxidizing than the condensed species, then the metal-bearing gas will have a *lower* vapor pressure at the melt-vapor interface (Sossi et al., 2016; Sossi and Fegley, 2018).

As this study is only concerned with reduced starting conditions (below the IW buffer) for the melt, the oxygen-bearing gas species produced during congruent evaporation yields a vapor that is inherently more oxidizing than the condensed phase-

most significantly so at an fO_2 of IW-5. The result: an increasingly lower vapor pressure at the melt-vapor interface, which encourages phase change to vapor and increases the rate of evaporation. A reduction in oxygen fugacity also leads to higher degrees of $\delta^{25}Mg$, and $\delta^{29}Si$ isotope fractionation. This is a direct result of the decreased vapor pressure with a decreased fO_2 described above. The (relatively) more oxidizing gas associated with more reducing conditions creates lower vapor pressure that not only encourages evaporation rates, but also allows the increased escape of lighter isotopes to the vapor phase, leaving a more highly fractionated melt residue.

Oxygen fugacity also affects the final oxide abundances (Wt. %) in the melt residues upon completion of the model, with a maximum of 10.7 Wt. % difference between the model ran at an fO_2 of IW-1 and the model ran at an fO_2 of IW-5 (Figure 4.8). Meaning, that oxygen fugacity not only controls the rate of evaporation of major oxide components, but it also controls their relative volatilities. The models all show a volatility order of $Na_2O > FeO > SiO_2 > MgO > Al_2O_3 > CaO$, which reflects the order of volatility in silicate melts described by Sossi and Fegley (2019). However, this order disagrees with the volatility order of $Na > Si > Fe > Mg > Ca > Al$ expected based on the condensation temperatures described by Wood et al. (2018).

The control of oxygen fugacity on volatility is also evident in the X-Y normalized graphs showing weight percent vs. time (Figure 4.9). All graphs show a “switch” in MgO and SiO_2 volatility at some point during evaporation. This is also consistent with the relationship described by Sossi and Fegley (2019): while SiO_2 is more volatile than MgO and will indeed begin vaporizing first, as evaporation proceeds the activity coefficient of SiO_2 decreases. As a result, the partial pressure of SiO_2 in the melt falls below that of

MgO (Richter et al., 2002; 2007), yielding an observable exchange in their volatilities relative to one another. The models show that a change in oxygen fugacity has an obvious effect on this phenomenon. Although the same general volatility order is maintained at all oxygen fugacities, at more reducing conditions (lower f_{O_2}) this switch in volatility of SiO₂ and MgO happens earlier on the timescale of evaporation, and the resulting difference in abundance is more pronounced (i.e., there is a bigger difference in the partial pressures of SiO₂ and MgO at more reducing conditions).

In Figure 4.9, the switch in volatility occurs at time 0.78 for an oxygen fugacity of IW-1 at which point the normalized abundance of SiO₂ dips slightly below that of MgO, but the two remain quite similar for the remainder of evaporation. Alternatively, the switch in volatility occurs at time 0.49 for an oxygen fugacity of IW-5, at which point the normalized abundance of SiO₂ dips significantly below that of MgO, and the two exhibit notable differences for the remainder of the evaporation. This is reflected in the CaO and Al₂O₃ normalized abundances. CaO and Al₂O₃ do not experience evaporation and thus become increasingly concentrated in the remaining melt upon increased volatilization of other compounds (MgO in this case). Since this SiO₂-MgO volatility relationship is governed by the activity of SiO₂ (Sossi and Fegley, 2019), and the activity of MgO is constant in this study, it is clear that oxygen fugacity has a significant impact of the activity of SiO₂.

5.3 Discussion of Activity Coefficient of MgO

It is clear in the models from runs 10-15 that the activity coefficient of MgO has a significant impact on the relative abundances of the major Earth-building oxides in this study. With all else equal, MgO, SiO₂, and FeO (the major constituents of the starting

chondrites) were all significantly impacted by a change in the activity coefficient of MgO. Al₂O₃, CaO, and Na₂O on the other hand, remain unchanged (Figure 4.12). While this demonstrates that in silicate melts at accretionary conditions, Al₂O₃, CaO, and Na₂O are more or less compositionally independent of MgO, FeO, and SiO₂, it does not support the claim from Wood & Wade (2013) that FeO has the same weak compositional dependence.

Direct relationships between the activity of MgO and the resulting activities of FeO and SiO₂ can be deduced from the models. For FeO, a higher activity coefficient of MgO (0.7) hinders the volatility of FeO, causing more FeO to be retained in the melt, and vice versa. This is clearly demonstrated in Figure 4.11, where the Fe/Mg activity ratio (slope) is larger for lower activity coefficients for MgO, and smaller for higher activity coefficients of MgO. The opposite relationship is observed for SiO₂; an increase in the activity coefficient for MgO encourages volatile behaviour of SiO₂ and causes a more silica-depleted melt. This is explained by the SiO₂-MgO relationship previously described. Since the activity coefficient of SiO₂ is known to drop below that of MgO sometime after the start of evaporation, a higher activity coefficient for MgO will amplify this effect, and vice versa.

5.4 Discussion of f_{O_2} Modified KNFCMAS Model for Sample Analysis

The f_{O_2} Modified KNFCMAS Model has proven to be an extremely effective means for isolating singular factors involved in the evaporation of simplified enstatite chondrites. It has been demonstrated that the model can be successfully used to determine unknowns in experimental environments. In this case, the unknowns were the activity coefficient of MgO during evaporation of the synthetic chondrites, and the effective

pressure experienced by the synthetic chondrites during the evaporation experiments. By comparing the experimental data to computational models reflecting the experimental conditions, a trendline for an activity coefficient of MgO much smaller than 1 is observed (Figure 4.13). There is still significant uncertainty involved with using the f_{O_2} Modified KNFCMAS Model to quantify the true activity of MgO in experimental melts, which is evident in the slope uncertainty of 0.685 in the trendline through the experimental data (Figure 4.13). This is because the model uses a set activity coefficient for MgO throughout the entire course of evaporation, which does not accurately reflect natural melts. As previously mentioned, the activity coefficient of MgO will change as the melt composition evolves, rather than remain constant. Nevertheless, the results show that an activity coefficient of 1 for MgO (the value for an ideal gas), which is the value commonly used in models for silicate melt-vapor systems, is an overestimation. This not only gives valuable insight into the chemistry of our samples, but also emphasizes the importance of ascertaining an appropriate model for the activity coefficient of MgO in silicate-melt vapor calculations.

When compared to the $\delta^{25}\text{Mg}$ and $\delta^{56}\text{Fe}$ values given by the f_{O_2} Modified KNFCMAS Model (set at the experimental conditions), a linear fit applied to the $\delta^{25}\text{Mg}$ and $\delta^{56}\text{Fe}$ data from the levitation experiments showed pressures consistent with model runs significantly lower than 1.00 bar (Figure 4.14). This linear fit demonstrates an effective pressure experienced by the spheres. This effective pressure is approximated to be between 0.1 bar and 0.01 bar, which significantly differs from the ambient pressure in the levitation chamber (1.00 bar), meaning that the evaporative flow surrounding the levitating spheres causes a low-pressure effect. This effect is likely from the levitation

gas removing evaporated species upon vaporization, which simulates lower pressures. However, to quantify and better understand the effect of the levitation gas on the effective pressure, a model considering both diffusive and advective evaporation is needed. The version of the fO_2 Modified KNFCMAS Model used in this study only considers diffusive evaporation, however some degree of advection (transport of evaporated species with fluid flow) is inevitable with the flow of levitation gas around the evaporating sphere.

5.5 Suggestions for Future Work

This study demonstrates the significant effects that varying activity coefficients have on chondrite chemistry. However, activity coefficients are extremely complex and while a full, comprehensive study of the individual activity coefficients for major elements in silicate melts during accretionary conditions is necessary, it was outside the scope of this study. To further our understanding of the chemical evolution of planetesimals, an activity-isolated study should be done. Further modifications to the fO_2 Modified KNFCMAS Model that enables manipulation of the activity coefficients for FeO, SiO₂, and MgO upon input would provide an ideal follow up to this study.

As previously mentioned, one of the main arguments for using the fO_2 Modified KNFCMAS Model for this study is that it models evaporation from a shrinking sphere, while other commonly used models only consider a flat surface/interface. When considering pebbles and planetesimals, (relatively) small rocky bodies, it is important to consider that there are multiple effects that can alter the kinetics of an evaporating sphere; the curvature effect (Brune, 2020) and the size-dependent return flux effect (Tang and Young, 2021). A logical next step would be to expand on this concept and use the fO_2

Modified KNFCMAS Model for a size-isolated study of evaporating planetesimals. This could provide great insight into the effect of size on the mechanics of planetesimal evaporation as well as emphasize the importance of considering size and curvature in these studies. Furthermore, the potential effect that size has on pebble/planetesimal chemistry could expose the degree of significance that pebbles and/or planetesimals play in planet formation, and how much responsibility they hold for final planetary signatures.

5.6 Conclusions

Several major conclusions can be drawn from this study. Firstly, the total pressure of the evaporation environment influences both the rate of evaporation and the degree of fractionation experienced by chondritic pebbles/planetesimals. With a lower total pressure in the evaporation environment, there will be an associated increase in vaporization rate and a higher degree of isotope fractionation. Pressure has a direct influence over isotope signatures that result from planetesimal evaporation. The total pressure does not, however, have a large impact on the relative volatilities of oxides in a KNFCMAS melt, or on the final oxide composition following evaporation.

Secondly, it can be concluded that out of the variables studied, oxygen fugacity has the most influence on chondrite pebble/planetesimal chemistry during evaporation. Oxygen fugacity influences the rate of vaporization, the degree of isotope fractionation, the relative volatility of major oxides and the final oxide compositions of the melt residues. More reducing environments (lower fO_2) facilitate faster rates of vaporization and higher degrees of isotope fractionation, thus directly influencing the isotopic signatures of pebbles/planetesimals. More reducing environments lower the activity of SiO_2 , altering the relative volatilities of SiO_2 and MgO , and changing the final oxide

composition following evaporation. This study concludes, with complete agreement to Sossi and Fegley (2018), that under controlled temperature and pressure conditions, oxygen fugacity will control evaporation.

Thirdly, it can be concluded that for silicate melts under accretionary conditions, such as those simulated in this study, the activity coefficient of MgO has a significant effect on FeO, SiO₂, and MgO abundances— major Earth-building oxides— and should not be assumed to be 1. For these conditions, an activity coefficient much smaller than 1 for MgO is more accurate. Assuming an activity coefficient for MgO of 1 can result in poor predictions of major oxide compositions.

Lastly, it can be concluded that the f_{O_2} Modified KNFCMAS Model presents a more accessible way of studying cosmochemical processes, such as planetesimal evaporation. Through the application of this model, individual factors in pebble/planetesimal evaporation environments can be isolated and studied. In addition, this model proves to be a valuable experimental tool, as it can be used to compare to experimental data and determine unknowns in the experimental environment.

On a final note, this study demonstrates that the relative volatility of elements is indeed more complex than a definition based singularly on condensation temperature implies. It is shown that oxygen fugacity and activity coefficients can alter the relative volatility of elements, suggesting that relative volatilities are conditional and are affected by environmental factors and the other species present. The processes that rocky bodies experience in protoplanetary disks are complex and inaccessible, making them difficult to investigate. As a whole, this study provides a more accurate and comprehensive way of studying these processes.

APPENDICIES

Appendix A: Raw f_{O_2} Modified KNFCMAS Model Data: Pressure Series

See attached file.

Appendix B: Raw f_{O_2} Modified KNFCMAS Model Data: Oxygen Fugacity Series

See attached file.

Appendix C: Raw f_{O_2} Modified KNFCMAS Model Data: Activity Coefficient Series

See attached file.

Appendix D: Raw MC-ICPMS Data from Levitation Experiments

See attached file.

REFERENCES

- Albarède F. (2011). Oxygen Fugacity. In: Gargaud M. et al. (eds.) *Encyclopedia of Astrobiology*. Springer, Berlin, Heidelberg.
- Alexander, C. (2002). Application of MELTS to kinetic evaporation models of FeO-bearing silicate melts. *Meteoritics and Planetary Science*, 37, 245-256.
- Andersen, K. (1992). Brook Taylor's Work on Linear Perspective A Study of Taylor's Role in the History of Perspective Geometry. Including Facsimiles of Taylor's Two Books on Perspective. *Sources in the History of Mathematics and Physical Sciences*, 10.
- Anisimov, S. (1968). Vaporization of metal absorbing laser radiation. *Soviet Physics JETP*, 27(1), 182-183.
- Bitsch, B., Izidoro, A., Johansen, A., Raymond, S. N., Morbidelli, A., Lambrechts, M., & Jacobson, S. A. (2019). Formation of planetary systems by pebble accretion and migration: growth of gas giants. *Astronomy & Astrophysics*, 623, 623.
- Brune, W. (2020). *Curvature Effect: Kelvin Effect*. METEO 300: Fundamentals of Atmospheric Science. <https://www.e-education.psu.edu/meteo300/>
- Carmichael, I. S. E., Nicholls, J. T., & Smith, A. L. (1970). Silica activity in igneous rocks. *American Mineralogist: Journal of Earth and Planetary Materials*, 55 (1-2), 246-263.
- Carrera, D., Gorti, U., Johansen, A., & Davies, (M.). (2017). Planetesimal formation by the streaming instability in a photoevaporating disk. *The Astrophysical Journal*, 839(1), 16.

- de Vries, J., Nimmo, F., Melosh, J., Jacobson, S., Morbidelli, A. & Rubie, D. (2016). Impact-induced melting during accretion of the Earth. *Progress in Earth and Planetary Science*, 3(7), 11.
- Eun, C. (2017). Effect of surface curvature on diffusion-limited reactions on a curved surface. *The Journal of Chemical Physics*, 147(18).
- Fairbridge R.W., Hetherington N.S. (1997) Chamberlin, thomas chrowder (1843–1928); chamberlin—moulton planetesimal hypothesis. In: Encyclopedia of Planetary Science. Encyclopedia of Earth Science. Springer, Dordrecht.
- Frost, R. (1991). Introduction to oxygen fugacity and its petrologic importance. *Reviews in Mineralogy and Geochemistry*, 25(1-9).
- Geankoplis, C., Hersel, A. & Lepek, D. (2018). Introduction to Engineering Principles and Units. In *Transport Processes and Separation Process Principles (5th Edition)*. Pearson.
- Hin, R. C., Coath, C. D., Carter, P. J., Nimmo, F., Lai, Y. J., von Strandmann, P., Willbold, M., Leinhardt Z., Walter, M., & Elliott, T. (2017). Magnesium isotope evidence that accretional vapour loss shapes planetary compositions. *Nature*, 549(7673), 511-515.
- Javoy, M., Kaminski, E., Guyot, F., Andrault, D., Sanloup, C., Moreira, M., Labrosse, S., Jambon, A., Agrinier, P., Davaille, A. & Jaupart, C. (2010). The chemical composition of Earth: Enstatite chondrite models. *Earth and Planetary Science Letters*, 293, 259-268.

- Johansen, A., & Lacerda, P. (2010). Prograde rotation of protoplanets by accretion of pebbles in a gaseous environment. *Monthly Notices of the Royal Astronomical Society*, 404(1), 475-485.
- Johansen, A. & Lambrechts, M. (2017). Forming Planets via Pebble Accretion. *Annual Review of Earth and Planetary Sciences*, 45, 359-87.
- Keil, K. (2012). Angrites, a small but diverse suite of ancient, silica-undersaturated volcanic-plutonic mafic meteorites, and the history of their parent asteroid. *Geochemistry*, 72(3), 191-218.
- Kendall, C. & Caldwell, E. (1998). Chapter 2- Fundamentals of Isotope Geochemistry. In C. Kendall & J. McDonnell (Eds.), *Isotope Tracers in Catchment Hydrology* (pp. 51-86). Amsterdam, NL: Elsevier Science.
- Kreutzberger M. E., Drake M. J. & Jones J. H. (1986) Origin of the Earth's Moon: constraints from alkali volatile trace elements. *Geochimica et Cosmochimica Acta*, 50, 91-98.
- Levine, I. (2019). "Activity (Thermodynamics)." *AccessScience*, McGraw-Hill Education. Retrieved from <https://doi.org/10.1036/1097-8542.009500>.
- Lodders, K. (2003). Solar system abundances and condensation temperature of the elements. *The Astrophysical Journal*, 591, 1220-1247.
- Macris, C., Young, E., Manning, C. (2013). Experimental determination of equilibrium magnesium isotope fractionation between spinel, forsterite and magnesite from 600 to 800 °C. *Geochimica et Cosmochimica Acta*, 118, 18-32.

- McCoy, T. J., Dickinson, T. L., & Lofgren, G. E. (1999). Partial melting of the Indarch (EH4) meteorite: A textural, chemical, and phase relations view of melting and melt migration. *Meteoritics & Planetary Science*, 34(5), 735-746.
- McNaught, A. & Wilkinson, A. (1997). IUPAC. Compendium of Chemical Terminology, 2nd ed. *Blackwell Scientific Publications, Oxford*.
- Morse, H. (1910). On evaporation from the surface of a solid sphere. *Proceedings of the American Academy of Arts and Sciences*, 45(14), 363-367.
- Nitkiewicz, A., & Sterner, S. M. (1988). An improved Bond air mill for the preparation of spherical single crystals. *American Mineralogist*, 73(5-6), 662-666.
- Norris, C. A., & Wood, B. J. (2017). Earth's volatile contents established by melting and vaporization. *Nature*, 549(7673), 507-510.
- Paniello, R. C., Day, J. M., & Moynier, F. (2012). Zinc isotopic evidence for the origin of the Moon. *Nature*, 490(7420), 376-379.
- Powell, R. (1978). Equilibrium thermodynamics in petrology: An introduction. (1st ed.) Harper & Row.
- Pringle, E., Moynier, F., Savage, P., Badro, J. & Barrat, J. (2014). Silicon isotopes in angrites and volatile loss in planetesimals. *Proceedings of the National Academy of Sciences*, 111(48).
- Safronov, V. S., & Zvjagina, E. V. (1969). Relative sizes of the largest bodies during the accumulation of planets. *Icarus*, 10(1), 109-115.
- Schaefer, L., & Fegley Jr, B. (2004). A thermodynamic model of high temperature lava vaporization on Io. *Icarus*, 169(1), 216-241.

- Shahar, A. & Young, E.D. (2007). Astrophysics of CAI formation as revealed by silicon isotope LA-MA-ICPMS of an igneous CAI. *Earth and Planetary Science Letters*, 257, 497-510.
- Sikdar, J. & Rai, V.K. (2020) Si-Mg isotopes in enstatite chondrites and accretion of reduced planetary bodies. *Sci Rep*, 10(1273).
- Sossi, P. & Fegley, B. (2018) Thermodynamics of Element Volatility and its Application to Planetary Processes. *Reviews in Mineralogy & Geochemistry*, 84(1), 393-459.
- Sossi, P., Nebel, O., O'Neill, H. & Moynier, F. (2018). Zinc isotope composition of the Earth and its behaviour during planetary accretion. *Chemical Geology*, 477, 73-84.
- Sossi, P., Klemme, S., O'Neill, H., Berndt, J. & Moynier, F. (2019). Evaporation of moderately volatile elements from silicate melts: experiments and theory. *Geochimica et Cosmochimica Acta*, 260, 204-231.
- Takata, S., Sone, Y., Lhuillier, D. & Wakabayashi, M. (1998). Evaporation from or condensation onto a sphere: Numerical analysis of the Boltzmann equation for hard-sphere molecules. *Computers & Mathematics with Applications*, 35(1-2), 193-214.
- Tang, H. & Young, E.D. (2021). *Planetary Evaporation*. Manuscript submitted for publication.
- Taylor, S. (2001). *Solar System Evolution: A New Perspective*. Cambridge: Cambridge University Press.

- Tsuchiyama A., Nagahara H. & Kushiro I. (1981) Volatilization of sodium from silicate melt spheres and its application to the formation of chondrules. *Geochimica et Cosmochimica Acta*, 45, 1357–1367.
- Visscher, C. & Fegley, B. (2013). Chemistry of impact generated silicate melt-vapor debris disks. *The Astrophysical Journal Letters*, 667(L12).
- Youdin, A. & Goodman, J. (2005). Steaming instabilities in protoplanetary disks. *The Astrophysical Journal*, 620, 459-469.
- Wood, B. J., & Wade, J. (2013). Activities and volatilities of trace components in silicate melts: a novel use of metal–silicate partitioning data. *Contributions to Mineralogy and Petrology*, 166(3), 911-921.
- Wang, K., & Jacobsen, S. B. (2016). Potassium isotopic evidence for a high-energy giant impact origin of the Moon. *Nature*, 538(7626), 487-490.
- Weber, R., Felten, J. & Nordine, P. (1996). Laser hearth melt processing of ceramic materials. *Review of Scientific Instruments*, 67(522).
- Weidenschilling, S. J. (1977). The distribution of mass in the planetary system and solar nebula. *Astrophysics and Space Science*, 51(1), 153-158.
- Weisberg, M. K., McCoy, T. J., & Krot, A. N. (2006). Systematics and evaluation of meteorite classification. In D. S. Lauretta & H. Y. McSween (Eds.). *Meteorites and the early solar system II* (pp. 19-52). University of Arizona Press.
- Young, E. D. (2017). Evaporating Planetesimals. *Nature*, 549. 461-462.
- Young, E. D., Nagahara, H., Mysen, B. & Audet, D. (1998). Non-Rayleigh oxygen isotope fractionation by mineral evaporation: Theory and experiments in the system SiO₂. *Geochemica et Cosmochemica Acta*, 62(18), 3109-3116.

Young, E. D., Shaha, A., Nimmo, F., Schlichting, H. E., Schauble, E. A., Tang, H. & Labidi, J. (2019). Near-equilibrium isotope fractionation during planetesimal evaporation. *Icarus*, 323, 1-15.

Young, E. & Tang, H. (2019). Isotopic Fractionation of Moderately Volatile Elements During Moon Formation. In *Lunar and Planetary Science Conference* (Vol 50).

Zuckerman, E. (2014, January 23). *Evaporation, Vapor Pressure and Boiling* [Video].

YouTube. <https://www.youtube.com/watch?v=CfagHzOtIDM>

CURRICULUM VITAE
Arielle Ann Hogan

Education

- *Master of Science*
Major in Geology
Earned at Indiana University-Purdue University Indianapolis
2021
- *Bachelor of Science*
Major in Earth Sciences
Earned at Memorial University of Newfoundland
2019
- *Honors Diploma*
Earned at Holy Heart of Mary High School
2012

Professional Experience

- *Graduate Research Assistant*
CAM Experimental Geochemistry Laboratory
Indiana University-Purdue University Indianapolis
August 2019 – May 2021
- *Research Assistant*
Experimental Geochemistry Laboratory
Memorial University of Newfoundland
July 2018 – May 2019
- *Junior Geologist*
Aurion Resources
July 2016 – July 2018
- *Field Assistant*
Geological Survey of Newfoundland
May 2014 – August 2014

Awards

- *Memorial University of Newfoundland 50th Anniversary Scholarship*
- *Centenary of Responsible Government Scholarship*

Publications

Young, E., Macris, C., Tang, H., Hogan, A. & Shollenberger, Q. (2021). Isotope velocimetry: Experimental and theoretical demonstration of the potential importance of gas flow for isotope fractionation during evaporation of protoplanetary material. *Earth and Planetary Science Letters* [in review].